CHAPTER 2

LITERATURE REVIEW

2.1 Thermoelectric materials

Materials, with the efficient generation of power by the Seebeck effect or refrigerate by the Peltier effect, are known as thermoelectric materials. They are also able to act as solid state refrigerators or heat pumps, without having any moving parts or using environmentally harmful fluids. Due to the high reliability and simplicity, they are widely extensive use, such as space power generation and a variety of cooling applications [2].

2.1.1 Principles of thermoelectric energy conversion

Thermoelectric materials are capable of converting heat directly into electrical energy. They are based on the Seebeck effect, discovered by Thomas Johann Seebeck in 1821 [2,5]. He observed that when two dissimilar materials were joined together and the junctions were held at different temperatures (ΔT), a voltage difference (ΔV) develops which was proportional to the temperature difference as shown in Figure 2.1. The ratio of the voltage developed to the temperature gradient ($\Delta V/\Delta T$) is related to an intrinsic property of the materials, known as the Seebeck coefficient, α. The Seebeck coefficient is very low for metals (only a few μV/K) and much larger for semiconductors (typically a few hundred μV/K) [3]. The phenomenon of an electrical current induced by a temperature gradient was termed ''thermoelectricity" [2]. Physical properties of thermoelectricity have explained for

this phenomenon: mobile charge carriers (electrons or holes) at the hot side of the material have more thermal energy than carriers at the cold side, causing a net diffusion of mobile carriers to the cold side. Since there are more mobile carriers at the cold side than the hot side, the inhomogeneous charge distribution forms an electric field which opposes the diffusion. If the material is in an open circuit, equilibrium will be reached when the rate at which carriers diffuse from the hot side to the cold side is balanced by the rate at which carriers move from the cold side to the hot side, due to the electric field. Thus in equilibrium an electrochemical potential will form in response to a temperature gradient; this electrochemical potential is known as the Seebeck voltage. The amount of voltage generated per unit temperature gradient is called the Seebeck coefficient. If the material is connected to a circuit, the electrochemical potential will drive a current which can be used to perform electrical work, which is the fundamental for thermoelectric power generation [2], as shown in Figure 2.2. In Seebeck's case, the temperature gradient-induced electrochemical potential created a current in the circuit, causing the generation of a magnetic field around the current loop.

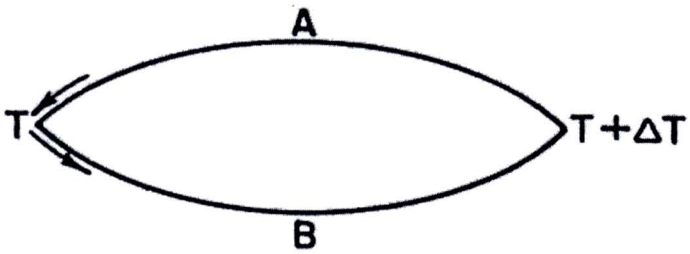

Figure 2.1 Thermodynamic circuit for the relative Seebeck coefficient [5].

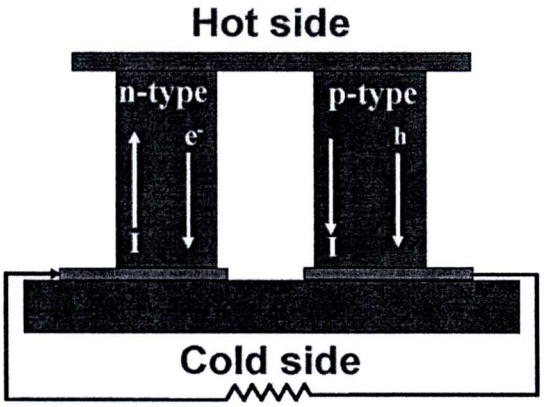

Figure 2.2 Schematic diagram of thermoelectric power generation [2].

Thermoelectrics can also be used as solid-state refrigerators or heat pumps by driving a current in a circuit with two dissimilar materials. This mode exploits the Peltier effect, discovered by Jean-Charles Peltier in 1834. Basically, heat is absorbed or rejected at the interface of two dissimilar materials, when a current flowed around a circuit as shown in Figure 2.3. This is explained by introducing the Peltier coefficient $\Pi=\alpha T$, which is a material dependent parameter, related to the Seebeck coefficient and described on how much thermal energy is carried per charge carrier. Since the heat current must be continuous across the interface of two materials. If the materials have different Peltier coefficients, heat will be either ejected or absorbed at the interface, depending on the sign of the difference between the Peltier coefficient and the direction of the current. If the current is injected in one direction the junction will extract heat, which is the basis for thermoelectric refrigeration. A current in the other direction will produce heat at the junction, and the device is acting as a heat pump. The rate at which the Peltier heat is liberated or rejected at the junction (Q_P) is given

by $Q_P = \alpha IT$, where I is the current through the junction and T is the temperature in Kelvin (K). Usually the two materials are chosen to be thermoelectric materials with the opposite majority carrier in Figure 2.4 (one n-type leg and one p-type leg) to maximize the difference between the Peltier coefficient and hence the amount of heat absorbed or generated [2,3].

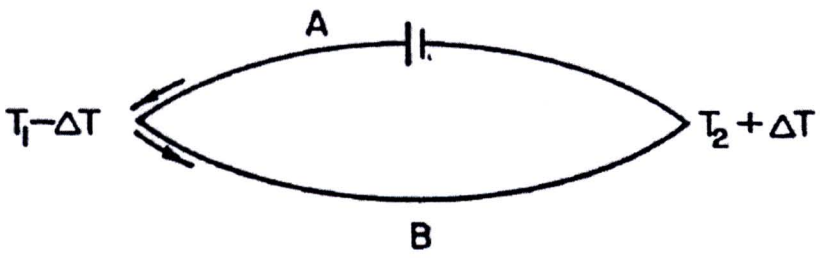

Figure 2.3 Thermodynamic circuit for the Peltier effect [5].

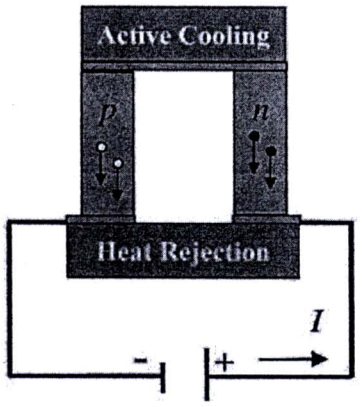

Figure 2.4 Schematic of thermoelectric refrigeration [3].

2.1.2 Definition and description of the figure of merit

The potential of a material for TE applications is determined in large part by a measure of the material's dimensionless figure of merit, ZT [3,8]:

$$ZT = \frac{\alpha^2 \sigma T}{\kappa} = \frac{\alpha^2 T}{\rho \kappa} \tag{2.1}$$

where α is the Seebeck coefficient, σ is the electrical conductivity, ρ is the electrical resistivity, and κ is the total thermal conductivity. The power factor, $\alpha^2\sigma$ (or α^2/ρ), is typically optimized in narrow-gap semiconducting materials as a function of carrier concentration (typically ~10^{19} carriers/cm^3), through doping, to give the largest *ZT*. High-mobility carriers are most desirable, in order to have the highest electrical conductivity for a given carrier concentration. The *ZT* for a single material is somewhat meaningless, since an array of TE couples is utilized in a device or module.

2.1.3 Conflicting thermoelectric material properties

Fundamental to the field of thermoelectric materials is the need to optimize a variety of conflicting properties. To maximize the thermoelectric dimensionless figure of merit (*ZT*) of a material, a large thermopower (absolute value of the Seebeck coefficient), high electrical conductivity, and low thermal conductivity are required. These transport characteristics depend on the interrelated material properties, a number of parameters needed to be optimized to maximize *ZT* [8].

1) Carrier concentration

To ensure that the Seebeck coefficient is large, there should only be a single type of carrier. Mixed *n*-type and *p*-type conductions will lead to both charge carriers moving to the cold end, cancelling out the induced Seebeck voltage. Low carrier concentration insulators and even semiconductors have large Seebeck

coefficients (Equation 2.2). However, low carrier concentration also results in low electrical conductivity (Equation 2.3). The interrelationship between carrier concentration and Seebeck coefficient can be explained by relatively simple models of electron transport. For metals or degenerate semiconductors (parabolic band, energy-independent scattering approximation) the Seebeck coefficient is given by:

$$\alpha = \frac{8\pi^2 k_B^2}{3eh^2} m^* T \left(\frac{\pi}{3n}\right)^{2/3} \tag{2.2}$$

where n is the carrier concentration, k_B is Boltzmann constant, h is Planck's constant and m^* is the effective mass of the carrier. The electrical conductivity (σ) and electrical resistivity (ρ) are related to n through the carrier mobility μ:

$$\frac{1}{\rho} = \sigma = ne\mu \tag{2.3}$$

Figure 2.5 shows the compromise between large thermopower and high electrical conductivity in thermoelectric materials that must be struck to maximize the figure of merit ZT. This peak typically occurs at carrier concentrations between 10^{19} and 10^{21} carriers per cm^3: depending on the material system, which falls in between common metals and semiconductors, concentrations found in heavily doped semiconductors. Maximizing the efficiency (ZT) of thermoelectric involves a compromise of thermal conductivity (κ; plotted on the y axis from 0 to a top value of 10 $Wm^{-1}K^{-1}$) and Seebeck coefficient (α; 0 to 500 $\mu V\ K^{-1}$) with electrical conductivity (σ; 0 to 5,000 Ω^{-}

$^{1}cm^{-1}$). Good thermoelectric materials are typically heavily doped semiconductors with a carrier concentration between 10^{19} and 10^{21} carriers per cm^3. The thermoelectric power factor a^2s maximizes at higher carrier concentration than ZT. The difference between the peak a^2s and ZT is greater for the lower-κ_{lat} materials.

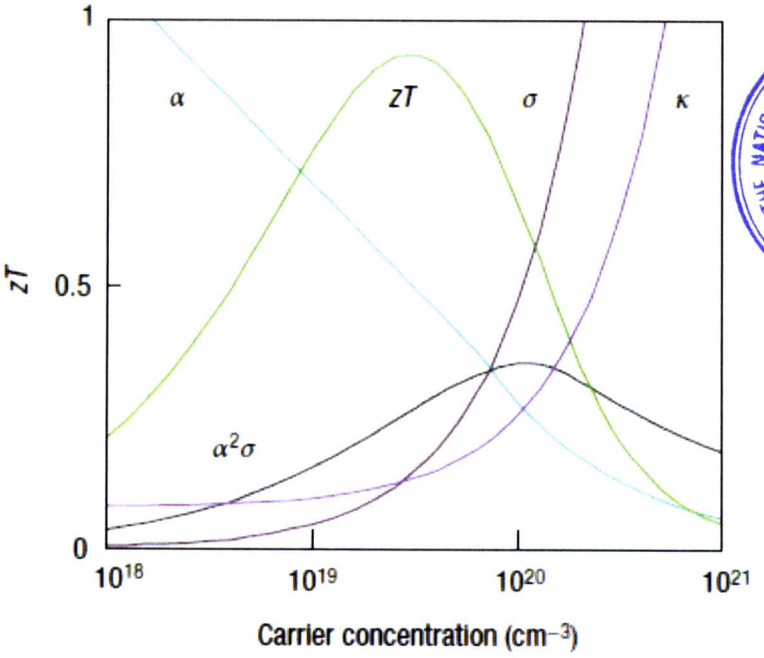

Figure 2.5 OptimizingZT through carrier concentration tuning[8].

2) Effective mass

The effective mass of the charge carrier provides another conflict as large effective masses produce high thermopower but low electrical conductivity. The m^* in Equation2.2 refers to the density-of-states effective mass, which increases with flat, narrow bands with high density of states at the Fermi surface. However, the inertial effective mass is also related to m^*, heavy carriers will move with slower velocities, and therefore small mobilities, which in turn leads to low electrical

conductivity (Equation 2.3). The exact relationship between effective mass and mobility is complex, depending on electronic structure, scattering mechanism and anisotropy. In principle, these effective mass terms can be decoupled in anisotropic crystal structures [5]. A balance must be found for the effective mass (or bandwidth) for the dominant charge carrier, forming a compromise between high effective mass and high mobility. High mobility and low effective mass is typically found in materials made from elements with small electronegativity differences, but high effective masses and low mobilities are found in materials with narrow bands such as ionic compounds. It is not obvious which effective mass is optimum; good thermoelectric materials can be found within a wide range of effective masses and mobilities: from low-mobility, high-effective-mass polaron conductors (oxides [24], chalcogenides [25]) to high-mobility, low-effective-mass semiconductors (SiGe, GaAs).

3) Electronic thermal conductivity

Additional materials design conflicts stem from the necessity for low thermal conductivity. Thermal conductivity in thermoelectrics comes from two sources: (1) electrons and holes transporting heat (κ_{el}) and (2) phonons travelling through the lattice (κ_{lat}). Most of the electronic term (κ_{el}) is directly related to the electrical conductivity through the Wiedemann–Franz law:

$$\kappa = \kappa_{el} + \kappa_{lat} \tag{2.4}$$

and

$$\kappa_{el} = L\sigma T = ne\mu LT \tag{2.5}$$

where L is the Lorenz factor, 2.4×10^{-8} J^2 K^{-2} C^{-2} for free electrons. The Lorenz factor can vary particularly with carrier concentration. Accurate assessment of κ_{el} is important, as κ_{lat} is often computed as the difference between κ and κ_{el} (Equations 2.4, 2.5) using the experimental electrical conductivity. A common source of uncertainty in κ_{el} occurs in low-carrier-concentration materials where the Lorenz factor can be reduced by as much as 20% from the free-electron value. Additional uncertainty in κ_{el} arises from mixed conduction, which introduces a bipolar term into the thermal conductivity. As this term is not included in the Wiedemann–Franz law, the standard computation of κ_{lat} erroneously includes bipolar thermal conduction. This results in a perceived increase in κ_{lat} at high temperature for Bi_2Te_3, PbTe and others, as shown in Figure 2.6. The onset of bipolar thermal conduction occurs at almost the same temperature as the peak in Seebeck and electrical resistivity, which are in accordance with bipolar effects.

As high ZT requires high electrical conductivity but low thermal conductivity, the Wiedemann–Franz law reveals an inherent materials conflict for achieving high thermoelectric efficiency. For materials with very high electrical conductivity (metals) or very low κ_{lat}, the Seebeck coefficient alone primarily determines ZT, as can be seen in Equation 2.6, where $(\kappa_{lat}/\kappa_{el}) << 1$:

$$ZT = \frac{\alpha^2/L}{1+\frac{\kappa_{lat}}{\kappa_{el}}} \tag{2.6}$$

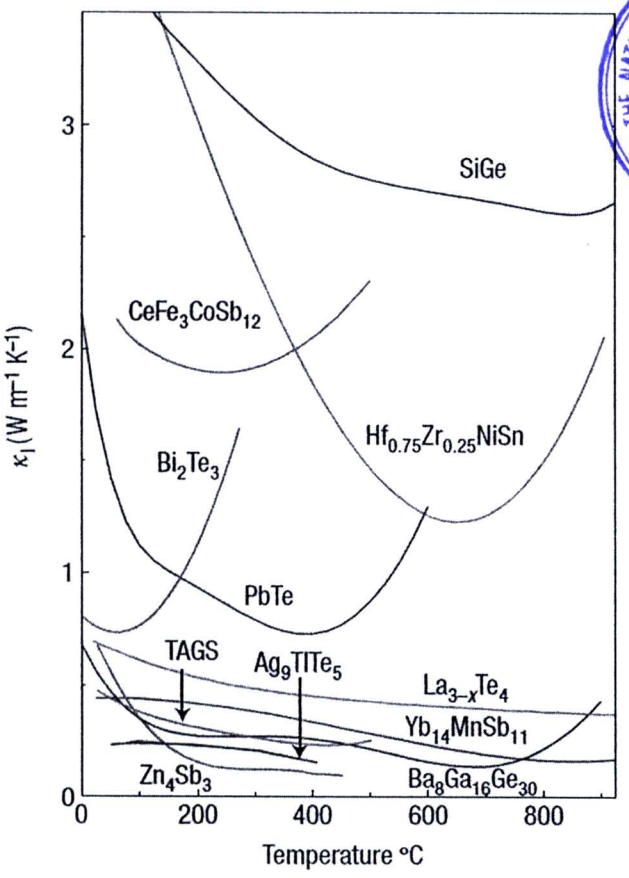

Figure 2.6 Complex crystal structures that yield low lattice thermal conductivity. Extremely low thermal conductivities are found in the recently identified complex material systems [8].

4) Lattice thermal conductivity

Glasses exhibit some of the lowest lattice thermal conductivities. For a glass, thermal conductivity is viewed as a random walk problem of energy through a lattice rather than rapid transport via phonons, leading to the concept of a minimum thermal conductivity, κ_{min} [26]. Actual glasses, however, make poor thermoelectrics because they lack the needed "electron-crystal" properties–compared with crystalline

semiconductors, which have lower mobility due to increased electron scattering and lower effective masses because of broader bands. Good thermoelectrics are therefore crystalline materials that manage to scatter phonons without significantly disrupting the electrical conductivity. The heat flow is carried by a spectrum of phonons with widely varying wavelengths and mean free paths (from less than 1 nm to greater than 10 μm), creating a need for phonon scattering agents at a variety of length scales. Thermoelectrics therefore require a rather unusual material: a "phonon-glass electron-crystal" (PGEC) [5]. The electron-crystal requirement stems from the fact that crystalline semiconductors have been the best at meeting the compromises required from the electronic properties (Seebeck coefficient and electrical conductivity). The phonon-glass requirement stems from the need of as low lattice thermal conductivity as possible. Traditional thermoelectric materials have used site substitution (alloying) with isoelectronic elements to preserve a crystalline electronic structure, while creating large mass contrast to disrupt the phonon path. Much of the recent excitement in the field of thermoelectrics is a result of the successful demonstration of other methods to achieve phonon-glass electron-crystal materials.

Figure 2.7 shows the reducing the lattice thermal conductivity leads to a two-fold benefit for the thermoelectric figure of merit. An optimized *ZT* of 0.8 is shown at point (1) for a model system (Bi_2Te_3) with a κ_{lat} of 0.8 $Wm^{-1}K^{-1}$, and κ_{el} that is a function of the carrier concentration (purple). Reducing κ_{lat} to 0.2 $Wm^{-1}K^{-1}$ directly increases the *ZT* to point (2). Additionally, lowering the thermal conductivity allows the carrier concentration to be reoptimized (reduced), leading to both a decrease in κ_{el} and a larger Seebeck coefficient. The reoptimized *ZT* is shown at point (3).

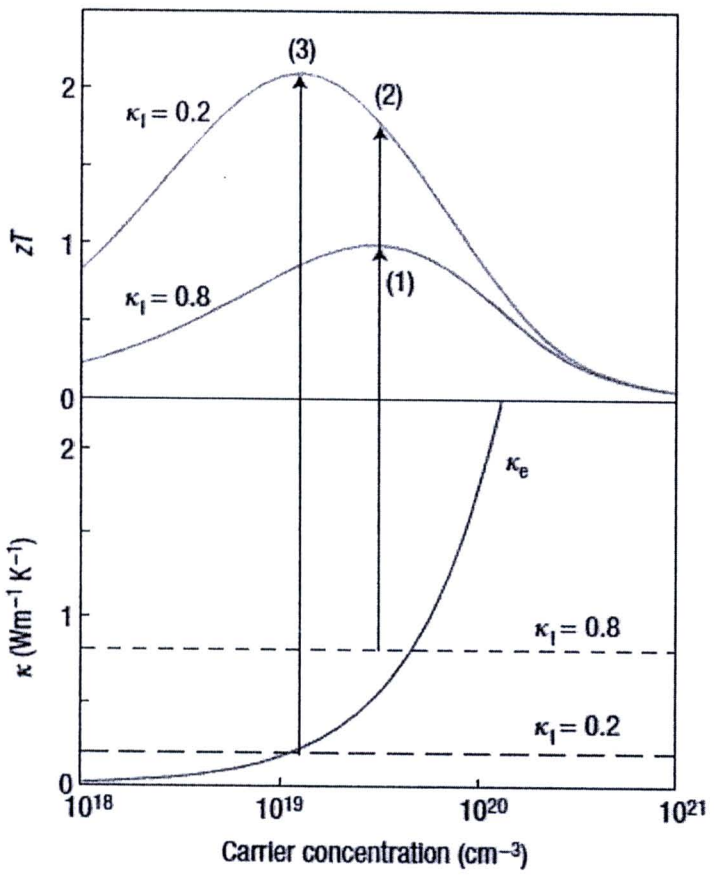

Figure 2.7 Reducing the lattice thermal conductivity leads to a two-fold benefit for the thermoelectric figure of merit [8].

5) Advances in thermoelectric materials

Renewed interest in thermoelectrics is motivated by the realization that complexity at multiple length scales can lead to new mechanisms for high *ZT* in materials [1,35]. In the mid 1990s, theoretical predictions suggested that the thermoelectric efficiency could be greatly enhanced by quantum confinement of the electron charge carriers. The electron energy bands in a quantum-confined structure are progressively narrower as the confinement increases and the dimensionality

decreases. These narrow bands should produce high effective masses and therefore large Seebeck coefficients. In addition, similar sized, engineered heterostructures may decouple the Seebeck coefficient and electrical conductivity due to electron filtering [36] that could result in high *ZT*. Even though a high-*ZT* device based on these principles has yet to be demonstrated, these predictions have stimulated a new wave of interest in complex thermoelectric materials. Vital to this rebirth has been interdisciplinary collaborations: research in thermoelectrics requires an understanding of solid-state chemistry, high-temperature electronic and thermal transport measurements, and the underlying solid-state physics. These collaborations have led to a more complete understanding of the origin of good thermoelectric properties. There are unifying characteristics in recently identified high-*ZT* materials that can provide guidance in the successful search for new materials. One common feature of thermoelectrics recently discovered with $ZT > 1$ is that most have lattice thermal conductivities with lower than the present commercial materials. Thus the general achievement is to get closer to a "phonon glass" while maintaining the "electron crystal". These reduced lattice thermal conductivities are achieved through phonon scattering across various length scales as discussed above. A reduced lattice thermal conductivity directly improves the thermoelectric efficiency, *ZT*, (Equation 2.6) and additionally allows re-optimization of the carrier concentration for additional *ZT* improvement (Figure 2.7).

There are three general strategies to reduce lattice thermal conductivity that have been successfully used. The first is to scatter phonons within the unit cell by creating rattling structures or point defects such as interstitials, vacancies or by alloying [5]. The second is to use complex crystal structures to separate the electron-

crystal from the phonon-glass. The goal is to be able to achieve a phonon glass without disrupting the crystalline of the electron-transport region. The third is to scatter phonons at interfaces, leading to the use of multiphase composites mixed on the nanoscale [1]. These nanostructured materials can be formed as thin-film superlattices or as intimately mixed composite structures.

2.1.4 Thermoelectric modules: devices

The Peltier effect is the basis for many modern-day TE refrigeration devices, and the Seebeck effect is the basis for TE power-generation devices. The versatility of TE materials is illustrated in Figure 2.8, which shows a TE couple composed of an *n*-type (negative thermopower and electron carriers), and a *p*-type (positive thermopower and hole carriers) semiconductor material connected through metallic electrical contact plates. Both refrigeration and power generation may be accomplished by the same module, as shown in Figure 2.8. A TE module or device is built up of an array of these couples, arranged electrically in series and thermally in parallel, as shown in Figure 2.8(c) and Figure 2.9. Thermoelectric energy conversion utilizes the Seebeck effect, wherein a temperature gradient is imposed across the device, resulting in a voltage that can be used to drive a current through a load resistance or device, as shown in Figure 2.8(b).

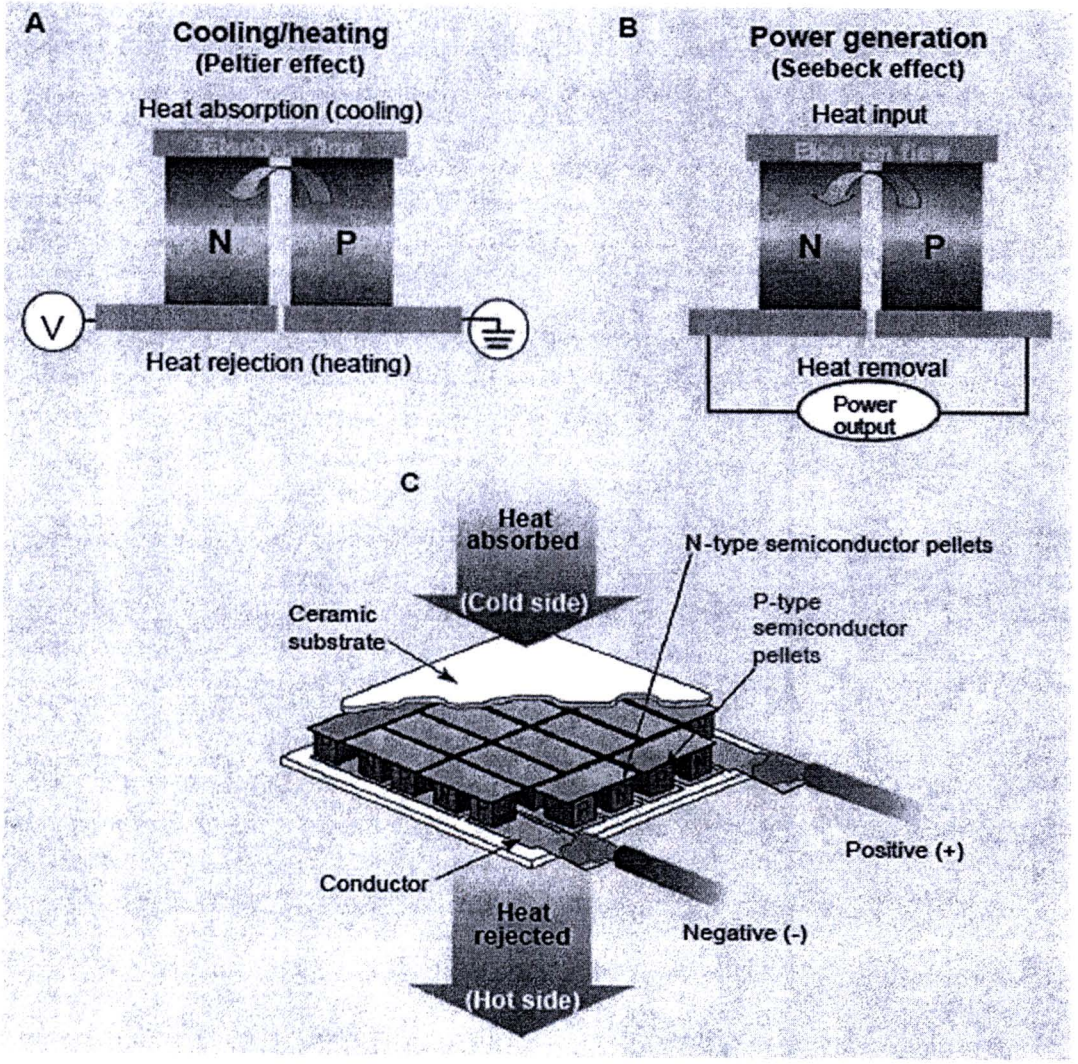

Figure 2.8 TE heat engines. (A) When current is run across a TE junction, it heats or cools through the Peltier effect, depending on the direction of the current flow. (B) When heat flows across the junction, electrical current is generated through the Seebeck effect. (C) Practical TE generators connect large numbers of junctions in series to increase operating voltage and spread heat flow [4].

This is the direct conversion of heat into electricity. Conversely, the Peltier heat generated when an electric current is passed through a TE material provides a

temperature gradient, with heat being absorbed on the cold side, transferred through (or pumped by) the TE materials, and rejected at the sink, thus providing a refrigeration capability. The advantages of TE solid-state energy conversion are compactness, quietness (static parts), and localized heating or cooling. In addition, energy in the form of waste heat (0% efficiency) that would normally be lost could be converted into useful electrical energy (≥7–8%), using a TE power-generation device.

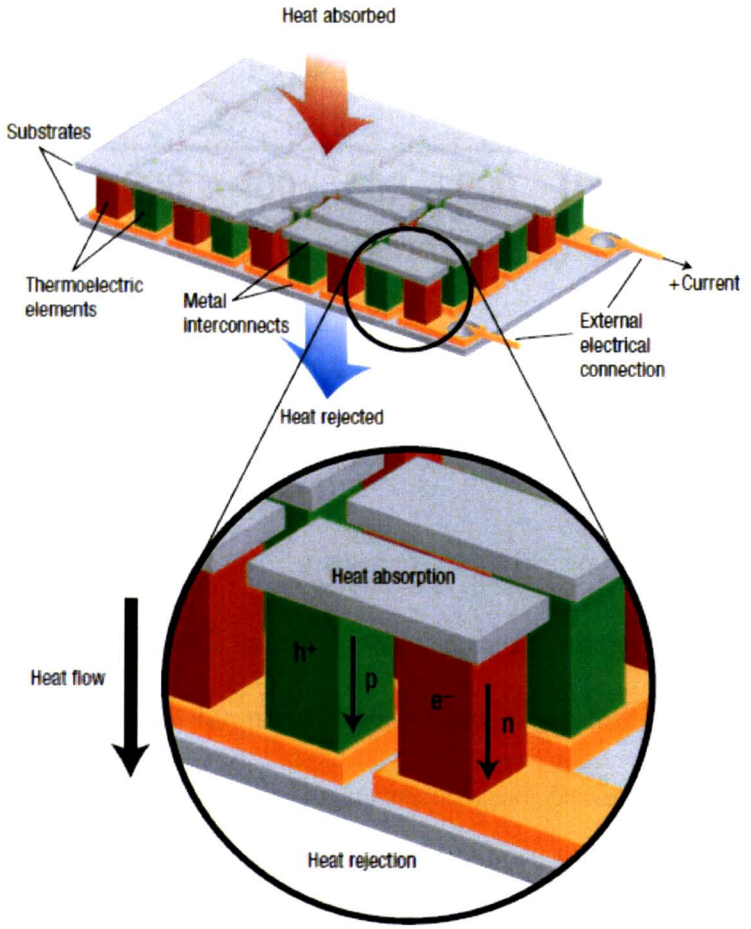

Figure 2.9 Thermoelectric module showing the direction of charge flow on both cooling and power generation [8].

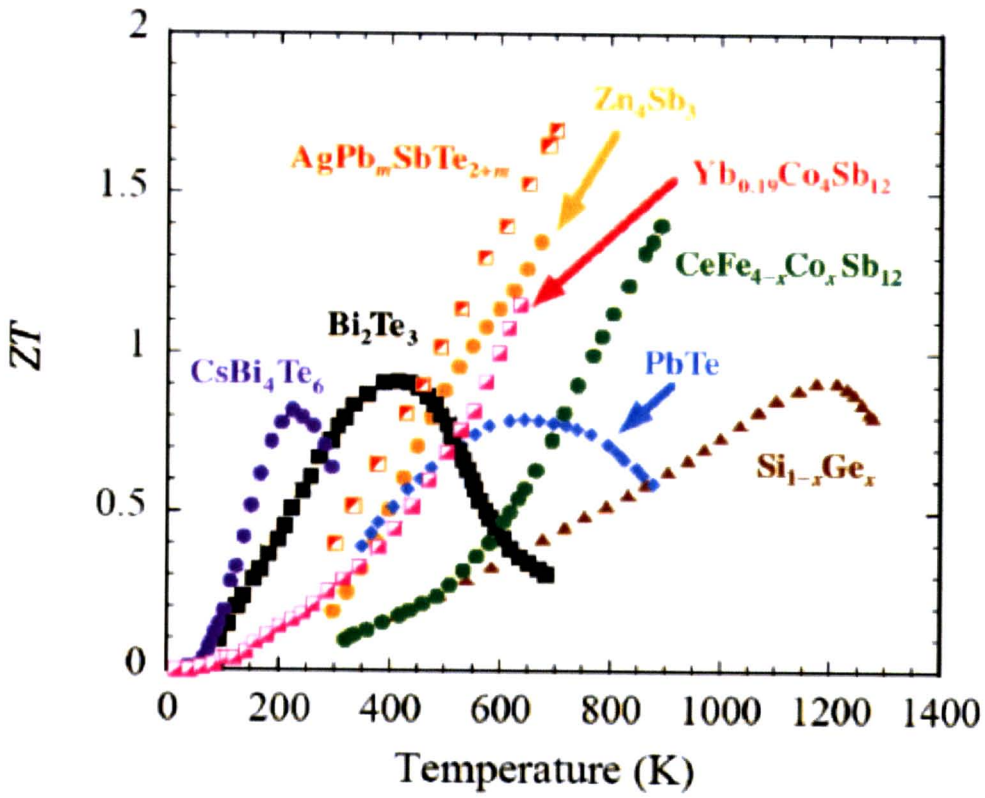

Figure 2.10 Dimensionless figure of merit ZT shown as a function of temperature for several bulk thermoelectric materials [3].

The best TE materials currently used in devices have $ZT \approx 1$. This value has been a practical upper limit for more than 30 years, yet there are no theoretical or thermodynamic reasons for $ZT \approx 1$ as an upper barrier. As seen from Equation2.1, ZT may be increased by decreasing κ_{lat} or by increasing either a or s. However, s is related to the electronic thermal conductivity, κ_{el}, through the Wiedemann–Franz relationship, and the ratio is essentially constant at a given temperature. These traditional TE materials have undergone extensive investigation, and there appears to be little room for future improvement in the common bulk structures. However, recent

results on nanostructures of traditional TE materials have shown a promising new direction for these materials. In addition, entirely new classes of compounds will have to be investigated. Figure 2.10 shows ZT as a function of temperature for the Bi_2Te_3 and $Si_{1-y}Ge_y$ materials as well as many of the more recent bulk materials that have been developed over the last decade.

2.1.5 Thermoelectric efficiency

There are two materials in the TE couple, as shown in Figures 2.8 and 2.9, an *n*-type and *p*-type. Ignoring parasitic contributions that reduce the device performance, such as contact resistance and radiation effects, the resulting dimensionless figure of merit for the couple (based solely on the TE materials) is given by

$$ZT = \frac{(\alpha_p - \alpha_n)^2 T}{\left[(\rho_n \kappa_n)^{1/2} + (\rho_p \kappa_p)^{1/2}\right]} \tag{2.7}$$

The coefficient of performance Φ (refrigeration mode), and the efficiency η (power generation mode) of the TE couple are directly related to the figure of merit shown in Equation 2.7 for the efficiency. The efficiency (η) of the TE couple is given by the power input to the load (W) over the net heat flow rate (Q_H), where Q_H is positive for heat flow from the source to the sink:

$$\eta = \frac{W}{Q_H} = \frac{T_H - T_C}{T_H}\left(\frac{(1+ZT_M)^{1/2} - 1}{(1+ZT_M)^{1/2} + (T_C/T_H)}\right) \tag{2.8}$$

where T_H is the hot-side temperature, T_C is the cold-side temperature, and T_m is the average temperature. Thus, one can see that η is proportional to $(1+ZT_m)^{1/2}$ and that the efficiency would approach the Carnot efficiency as ZT approaching infinity.

2.2 Microwave irradiation/heating

2.2.1 Dielectric heating [29]

Dielectric heating (also known as electronic heating, Radio frequency (RF) heating, high-frequency heating) is the process in which radio wave or microwave electromagnetic radiation heats a dielectric material. This heating is caused by dipole rotation. Molecular rotation occurs in materials containing polar molecules having an electrical dipole moment, which will align molecules in an electromagnetic field, as shown in Figure 2.11. If the field is oscillating, as an electromagnetic wave, these molecules rotate to continuously align with it, called dipole rotation. As the field alternates, the molecules will be induced to reverse their direction accordingly. Rotating molecules push, pull, and collide with other molecules (through electrical and gravitational forces), distributing the energy to adjacent molecules and atoms in the material as shown in Figure 2.12. Temperature is related to the average kinetic energy (energy of motion) of the atoms or molecules in the material - agitating the molecules in this way by the definitive increase of the temperature of the material. Dipole rotation is a mechanism by which energy in the form of electromagnetic radiation is converted to heat energy. There are other mechanisms by which this conversion occurs as well. Dipole rotation is the mechanism normally referred to as dielectric heating, and is most widely observable in the microwave oven. It operates

most efficiently on liquid water, and much less for on fats, sugars, and frozen water, because fats and sugars being far less polar than water molecules, and thus less affected by the forces generated by the alternating electromagnetic field. On the other hand, frozen water molecules are fixed in place in a crystal lattice and are not free to rotate, thus they cannot accelerate as much in response to the electromagnetic forces they experience in the external electromagnetic wave. Outside of cooking, the effect can be used to heat solids, liquids, or gases, provided that they contain some electric dipoles.

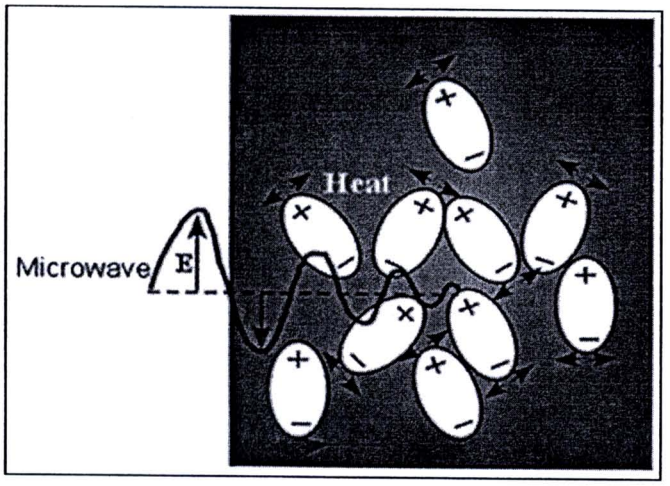

Figure 2.11 Dipole rotations of molecule occurs in materials containing polar molecules having an electrical dipole moment, which will align molecules in a microwave electromagnetic field.

For dielectric heating, the generated power density per volume follows the equation

$$P = \omega \cdot \varepsilon_r'' \cdot \varepsilon_0 \cdot E_{el}^{\ 2} \tag{2.9}$$

where ω is the angular frequency, ε_r'' is the imaginary part of the complex relative permittivity, ε_0 is the permittivity of free space, and E_{el} the electric field strength. The imaginary part of the complex relative permittivity is the potential performance of dielectric material to convert radio frequency electromagnetic field energy into heat.

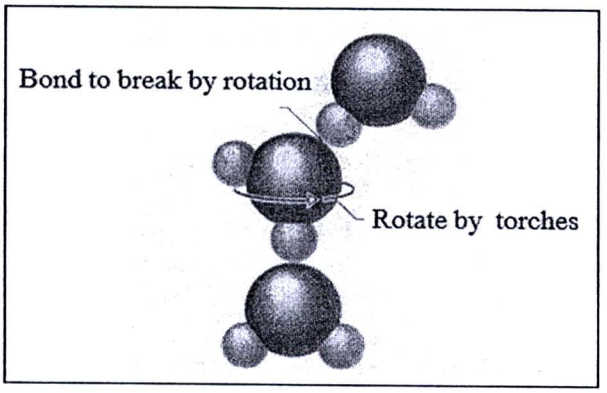

Figure 2.12 Molecular rotation for the generation of energy in the form of microwave electromagnetic radiation.

Communication microwave frequencies penetrate semi-solid substances to a distance proportional to their power density. The penetration stops essentially when all of the penetrating microwave energy has been converted to (absorbed as) heat in them. For this reason, it is dangerous to stand close to high-power microwave antennas such as those used for broadcasting over long distances (over 10 miles); a person around such antennas may experience severe penetrating burn, which (in the worst cases) may include serious burn injury to their organs inside. In the natural

sciences, the term diathermy means "electrically induced heat" and is commonly used for muscle relaxation. It is one of the methods of heating tissue electromagnetically or ultrasonically for therapeutic purposes in medicine. Ultrasonic diathermy refers to heating of tissues by ultrasound for the purpose of therapeutic deep heating. No tissue is ordinarily damaged hence it is generally used in biomedical applications. Electric diathermy uses high frequency alternating electric or magnetic fields, sometimes with no electrode or device contact to the skin, to induce gentle deep tissue heating by induction or dipole rotation.

2.2.2 Microwave plasma

Rao et al. (1999) listed the temperatures which the microwaves attenuated through a number of materials and inorganic compounds for different lengths of times, and summarized in Table 2.1. Several chalcogenides, such as cinnabar (HgS), molybdenite (MoS_2), orpiment (Ag_2S_3), sphalerite (ZnS), etc. also interact with microwaves but are not heated so rapidly as those listed in the Table [30].

Houmes et al. (1996) prepared recently a number of nitrides such as TiN, AlN, and GaN by the use of a plasma by exposing oxides to plasma of N_2/H_2 [31].

Houmes et al.(1997) reported microwave-assisted synthesis of binary (TiN, AlN, and VN) and ternary (Li_3FeN_2, Li_3TiN_2, Li_3AlN_2) nitrides by a direct reaction between metal powder and nitrogen by first striking a N_2 plasma for a low power microwave source as shown in Figure 2.13. Ternary nitrides were produced by direct reaction of either the component nitrides or a mixture of Li_3N and metal powder reacted in nitrogen plasma. It was noted that sustaining a plasma in the domestic

microwave oven is unfeasible. Microwave-generated N_2 plasma reactions were also used to demonstrate the formation of Si_3N_4 and BN [32].

Table 2.1 Microwave active elements, natural minerals, and compounds [30].

element/ mineral/ compound	Time (min) of microwave exposure	T, K	element/ mineral/ compound	Time (min) of microwave exposure	T, K
Al	6	850	NiO	6.25	1578
C (amorphous, < 1μm)	1	1556	V_2O_5	11	987
C (graphite, 200 mesh)	6	1053	WO_3	6	1543
C (graphite, < 1μm)	1.75	1346	Ag_2S	5.25	925
Co	3	970	Cu_2S (chalcocite)	7	1019
Fe	7	1041	$CuFeS_2$ (chalcopyrite)	1	1193
Mo	4	933	$Fe_{1-x}S$ (Phyrrhotite)	1.75	1159
V	1	830	FeS_2 (pyrite)	6.75	1292
W	6.25	963	MoS_2	7	1379
Zn	3	854	PbS	1.25	1297
TiB_2	7	1116	PbS (galena)	7	956
Co_2O_3	3	1563	CuBr	11	995
CuO	6.25	1285	CuCl	13	892
Fe_3O_4 (magnetic)	2.75	1531	$ZnBr_2$	7	847
MnO_2	6	1560	$ZnCl_2$	7	882

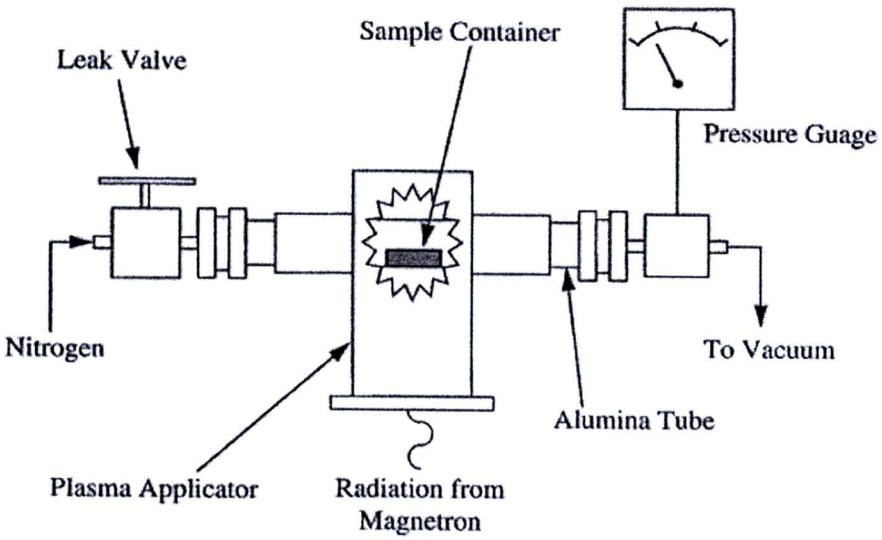

Figure 2.13 Schematic diagram of Cober microwave system used in the synthesis of binary nitride materials by exposing in a nitrogen plasma [32].

Douthwaite et al. (1996) reported a rapid synthesis of alkali metal fullerides by using microwave induced argon plasma. Reaction times appear to be only a few seconds while the conventional preparation takes a longer time. The microwave plasma was generated in argon held at a pressure of 10-5 mbar in evacuated quartz tubes. Fullerenes and alkali metals are kept physically separated, and the tube was at the position that the microwave amplitude was at the highest. The alkali metal quickly heated and vaporized, and the C_{60} reacted with condensed K under the Ar plasma. Under these conditions, K intercalated easily. It was also confirmed that uncondensed K in the plasma was not able to intercalate. It has been shown by alteration of reaction conditions that there was a thermal action of the plasma which was responsible for the rapid synthesis [33].

Cho et al. (2008) presented a microwave plasma torch system to a low-pressure chamber. The electric field induced in a quartz discharge tube by microwave radiation breaks down the gas at a sufficiently low pressure, igniting the plasma, which is continuously sustained by microwave radiation. The plasma profile at a very low pressure is shown to be asymmetric with higher density on the incoming side of the microwave. The plasma density increases as the microwave power increase. The typical argon plasma density of a plasma torch powered at 500 W under a pressure of 150 torr is on the order of $10^{14}/cm^3$. The electron temperature in the argon torch plasma was estimated to be 1.5 eV, thereby effectively exciting the molecules in the torch gas. Disintegration of nitrogen fluoride (NF_3) indicates that a microwave plasma torch operating at a low pressure can efficiently generate an abundant amount of chemical radicals [34].

Hong et al. (2005) have directly synthesized the N-doped titanium dioxide (TiO_2) particles of nanosize in an atmospheric microwave plasma-torch using gas-phase titanium tetrachloride ($TiCl_4$) [35].

Douthwaite et al. (2008) reported the rapid synthesis of alkali metal fullerides using a microwave induced argon plasma (MIAP). Reaction times are of the order of seconds using a MIAP, but conventional synthesis requires times of the order of several days [36].

Wu et al. (2000) presented the results of new 160-mm homogeneous plasmas produced at the pressure of 10-600 Pa. Homogeneous microwave plasmas have been produced and used for materials surface modification. Also, the axial distributions of plasma parameters have been investigated, with and without the short circuit at the top of the set-up, respectively. The experimental results showed that the

short circuit was efficient for the plasma density being raised and beneficial for plasma uniformity [37].

Shin et al. (2007) presented continuous wave (CW) microwave discharges to operate at atmospheric pressure in argon gas, which were applied to surface modification of metal surfaces for improvement of adhesion with pain coating as shown in Figure 2.14. The surface treatment was carried out by making use of the microwave discharges excited in a regular waveguide. The charged particles in the discharge plasma with high kinetic energy bombard the substrate, cleaning and etching its surface of rough morphology and polluted with organic compounds as shown in Figure 2.15 [38].

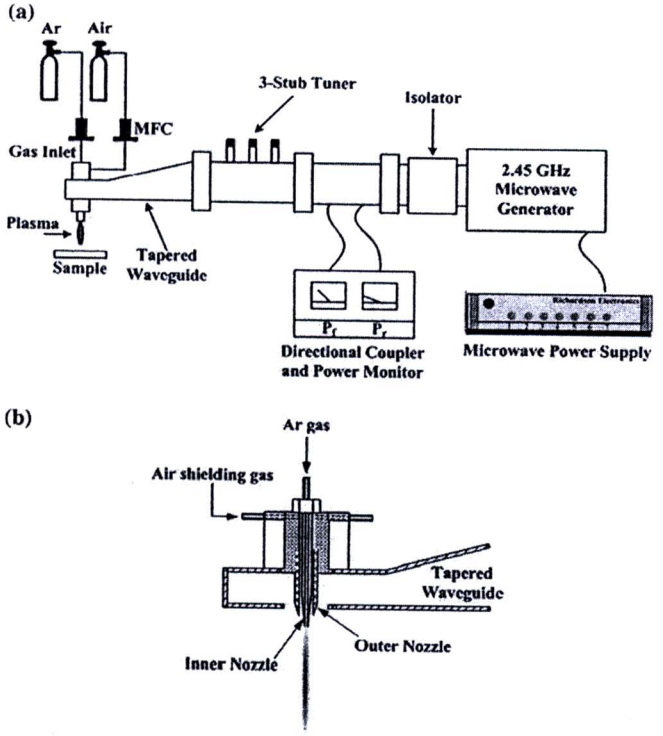

Figure 2.14 Schematic diagram of (a) the apparatus for plasma modification by making use of an atmospheric microwave plasma torch, and (b) the construction of the plasma nozzles [38].

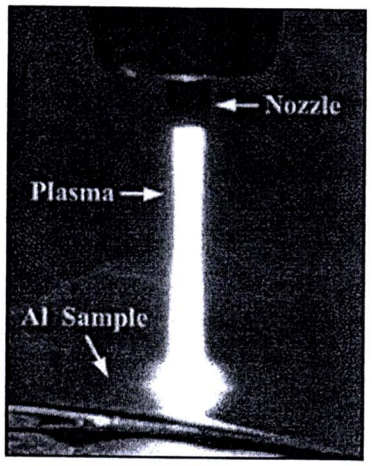

Figure 2.15 A photograph of the microwave plasma in operation for the treatment of Al sample [38].

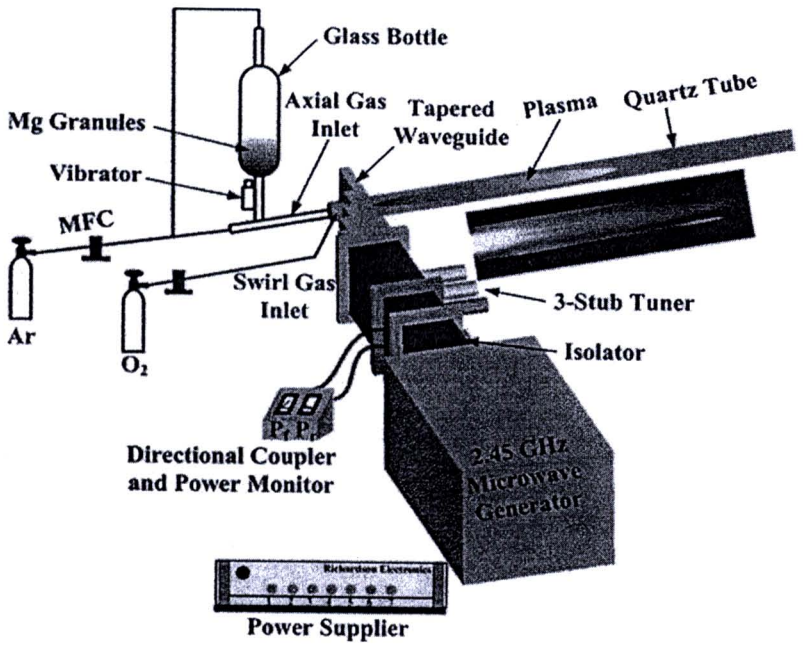

Figure 2.16 Schematic presentation for the synthesized system of MgO nanoparticles with the atmospheric microwave plasma torch. The inset shows the plasma emission of green color after completion of the synthesis [39].

Hong and Uhm (2006) have synthesized directly MgO nanopowders in torch flame of an oxygen microwave plasma using Mg granules as a source material. The plasma torch vaporized Mg granules immediately and Mg vapor was explosively oxidized, producing MgO powders as shown in Figure 2.16 [39].

Zhen et al. (2007) have been synthesized the high density, nanocrystalline Bi_2O_3-HfO_2-Y_2O_3 solid electrolyte by microwave plasma and pressure-less sintering as shown in Figure 2.17. After the samples were sintered by microwave plasma at 700 ^{o}C for 30 min, the relative density was found to be greater than 96%. Moreover, the sintered specimens exhibit considerably finer microstructure and denser, compared to that of the samples sintered by a conventional pressure-less condition [40].

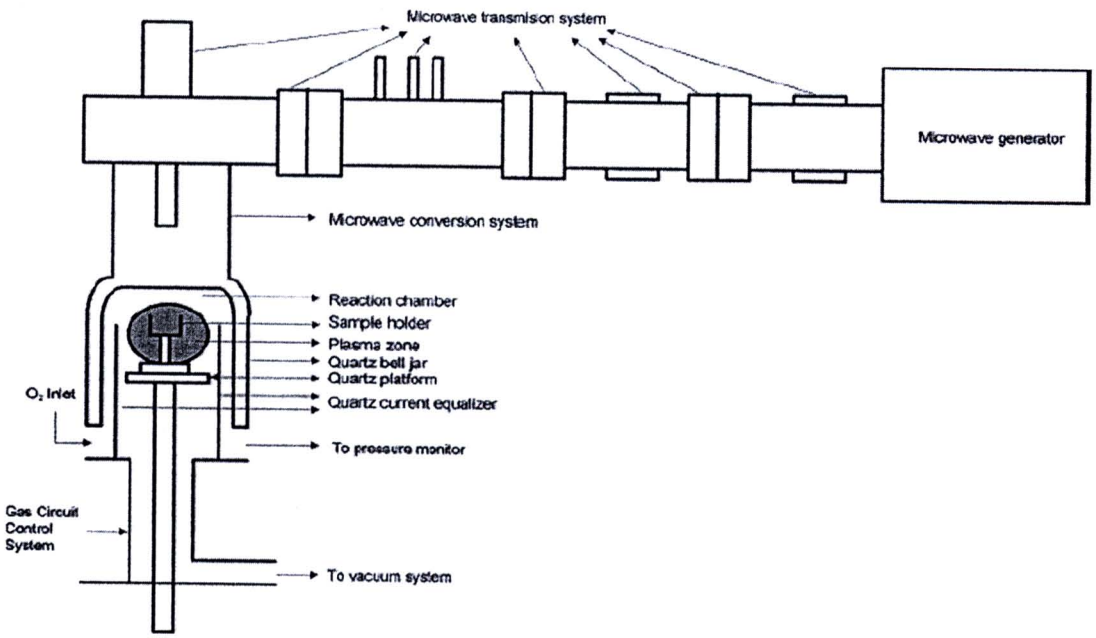

Figure 2.17 A schematic diagram of microwave plasma equipment [40].

Lekse et al. (2007) presented solid-state microwave synthesis, a viable method for the preparation of a wide variety of intermetallic compounds, such as Bi_2Pd and Ag_3In. This method contributes to a relatively new palette of several other nontraditional techniques, such as metal fluxes, mixed-metal eutectic fluxes, and solution methods, which provided convenient avenues toward the synthesis of intermetallics. Reaction times for solid-state microwave synthesis are greatly reduced, comparing to other synthetic methods. It was believe that it has real potential in this area because many of these intermetallic compounds are of technological interest. A quicker, greener synthetic method could be advantageous to these developments [41].

2.3 Solid-state reaction

A large variety of inorganic solids has been prepared by reacting a solid with another solid, a liquid (melt) or gas, usually at high temperature. When solid compounds are employed to react with each other at high temperatures, this does not necessarily imply that all components are still in the solid state at the temperatures required for reaction to occur. A liquid phase or even gaseous intermediates may involve in providing mass transport. The oldest and still most common method of preparing multicomponent solid materials is by direct reaction of solid components at high temperatures. Since solids do not react with each at room temperature-even, if thermodynamics favors product formation-high temperatures are necessary to achieve appreciable reaction rates. The advantage of solid-state reactions is the ready availability of the precursors and the low cost powder production on the industrial scale.

2.3.1 General aspects of solid-state reactions [42]

In order to understand the difference between reactions in solution and in the solid state, and the problems associated with solid-state reactions, the thermal reaction of two crystals of the compounds A and B which are in intimate contact across one face are considered (Figure 2.18). When no melt is formed during the reaction, it has to occur initially at the points of contact between A and B, and later by diffusion of the constituents through the product phase.

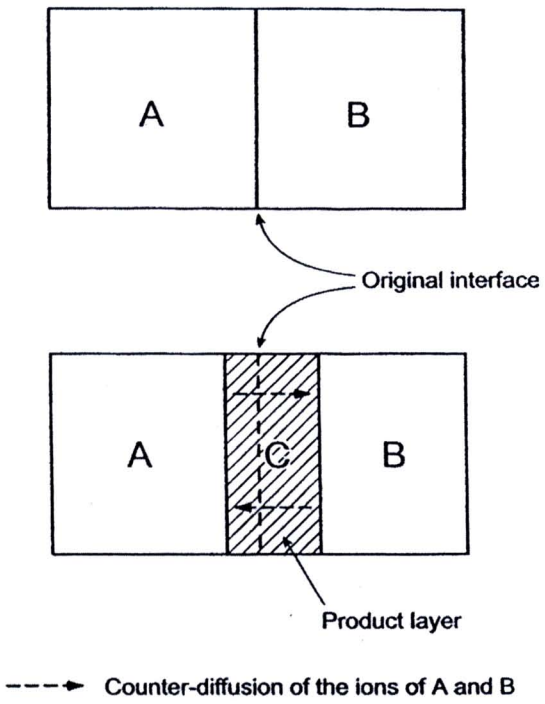

Figure 2.18 Reaction of two crystals (A and B) sharing one face. After initial formation of a product layer C, ions from A and B have to counter-diffuse through the product layer to from new product at the A/C and B/C interfaces [42].

The first stage of the reaction is the formation of nuclei of the product phase C at the interface between A and B. This may be difficult, if a high degree of structural reorganization is necessary to form the product. After nucleation of product C has occurred, a product layer is formed. At this stage, there are two reaction interfaces: between A and C, and between C and B. For further reaction to occur, counter-diffusion of ions from A and B must occur through the existing product layer C to the new reaction interfaces.

As the reaction progresses, the product layer becomes thicker. This results in increasingly longer diffusion paths and slower reaction rates, because the product layer between the reacting particles acts as a barrier. In the simple case where the rate of the reaction is controlled by lattice through a planar layer, the rate law has a parabolic from

$$\frac{dx}{dt} = k \cdot x^{-1} \qquad (2.10)$$

, where x is the thickness of the growing product layer, t is time, and k is the rate constant.

Ions are normally regarded as being trapped on their appropriate lattice sites. It is difficult for them to move to adjacent sites. Only at very high temperatures, the ions have sufficient energy to diffuse through the crystal lattice. As a rule of thumb, two-thirds of the melting temperature of one component is sufficient to activate diffusion sufficiently and hence to enable the solid-state reaction to proceed. There are there important factors that influence the rate of reaction between solids:

1. The area of contact between the reacting solids and hence their surface areas.
2. The rate of nucleation of the product phase.
3. Rates of diffusion of ions through the various phases and especially through the products phase.

Equation 2.10 relates the rate of solid-state reaction to the diffusion of ions through the bulk of the crystals and, especially through the product phase. Diffusion path lengths are influenced by the particle size of the reactants, the degree of homogenization achieved during mixing, and the intimacy of contact between the grains. Diffusion of ions is also enhanced greatly by the presence of crystal defects, especially and interstitials, but also occurs via structural defects such as dislocations and grain boundaries. In general, the rate of diffusion and the reactivity of solids depend greatly on the types of crystal defects.

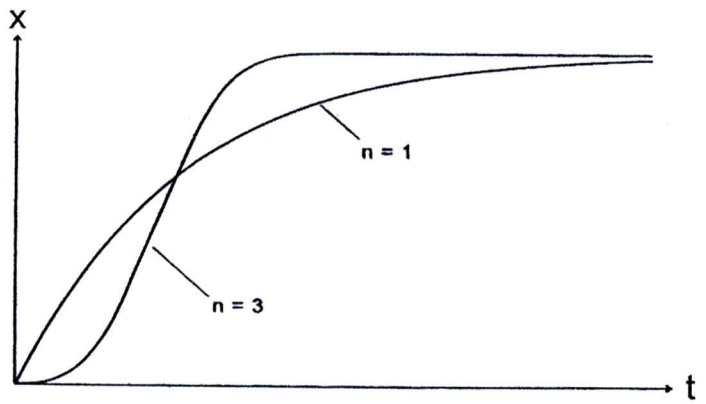

Figure 2.19 The relation of thickness and time for n = 1, and 3. The curve for n =3 graphically shows the induction period at the beginning of the reaction [42].

The overall process in solid-state reactions may not only to be controlled by diffusion of reactants, or by the rate of the reaction at the phase boundary, but also by nuclei growth. Nucleation limited reactions are represented by the Avrami-Erofeyev Equation (Equation 2.11 and Figure 2.19)

$$x(t) = 1 - e^{kt^n} \tag{2.11}$$

, where n is a real number, usually between 1 and 3. For $n > 1$, the function has a sigmoid shape. Initially a large number of nuclei are formed, and then the reaction front expands with the growth of the nuclei. When the resulting product regions touch each other, the reaction rate starts to decrease. Note that for most solid-state reactions, it is usually incorrect and misleading to think in terms of reaction order, since the reactions do not involve molecules. Nevertheless, the data may still be represented empirically in this way.

2.3.2 Formation of metastable solids [42]

Many metastable solids are of great current interest. Such compounds cannot be prepared by conventional high temperature routes. Thus alternative strategies have been developed. Low-temperature, chemistry-based approaches often allow a better control of the structure, stoichiometry, and phase purity. Metastable solids can be obtained by three different approaches:

1. Synthesis under conditions where the solids are thermodynamically stable, followed by quenching to ambient conditions.

2. Prefabrication of thermodynamically stable phase which then transformed to a metastable phase by a low-temperature, soft-chemical operation.
3. Synthesis under non-equilibrium conditions; the products are kinetically controlled metastable compounds.

2.4 Synthesis/alloying preparation

Due to a technological point of view, modern thermoelectric materials can be roughly divided into three categories: low-temperature materials (group V chalcogenides based on bismuth telluride), middle-temperature materials (group IV chalcogenides based on lead telluride), and high temperature materials (silicon-germanium solid solutions) [5,43]. The melting points and approximate total pressures of volatile elements over the melts of the major phases are shown in Table 2.2.

Table 2.2 Melting temperatures and total vapor pressures of major thermoelectric materials [43].

Temp. Range	Low-Temp. Materials			Middle-Temp. Materials				High-Temp. Materials
Material	Bi_2Te_3	Sb_2Te_3	Sb_2Se_3	PbTe	PbSe	GeTe	SnTe	$Si_{80}Ge_{20}$
T^M, °C	585	621	612	917	1076	725	806	1350
P^{tot}, torr at T^M	4	1	2	10	100	40	1	<< 1

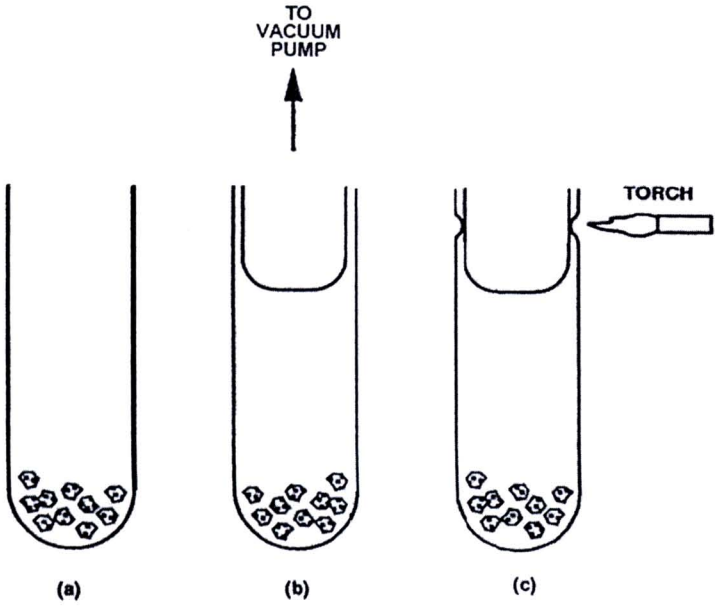

Figure 2.20 Synthesis/alloying ampoule preparation [5].

The preparation of chemical compounds and solid solutions from a melt begins with melting the elemental constituents together, a process referred to as synthesis or alloying. It is essential to use high-grade elements of guaranteed purity and to take all necessary precaution to prevent contamination during handling, synthesis, and crystal growth. A common way to synthesize the chalcogenides is to use sealed, clear quartz ampoules of up to 25-mm bore. The preweighed materials are placed into the tube (Figure 2.20a), followed by a quartz plug (Figure 2.20b). The tube is then evacuated and sealed circumferentially with a hydrogen torch (Figure 2.20c).

Before use, the quartz is usually washed in soapy water, cleaned with solvents (e.g., acetone, methanol), aqua regia (HNO_3 + 3HC1), and hydrofluoric acid (HF) diluted with high-purified water, rinsed in pure water, and dried. Most of the high-purified commercially available elements are oxidized on the surfaces. It is essential

to remove the oxides from the ingredients before synthesis, done by etching or by reduction of the elements. For example, lead placed in an alumina or graphite boat can be reduced at 700°C in a stream of pure hydrogen. The presence of oxygen causes the solidifying ingot to stick on the quartz walls, due to a chemical reaction between lead oxide and silica. This introduces stresses into the material and can even break the ampoule and expose the hot ingot to the air. In addition, any oxygen in the chalcogenides changes the electrical properties of the final products. To prevent sticking alone, quartz containers can be coated with carbon by pyrolitically cracking toluene in a nitrogen stream at 1050°C. The vibration may be used during processing to homogenize the melt [5].

2.5 Sintering [42]

When a compacted powder is heated at an elevated temperature which is below its melting point, powder particles fuse together. Voids between the particles decrease, and eventually a dense solid body is obtained. This phenomenon is called sintering. Sintering process have been used extensively for the manufacture of ceramics ironware for hundreds years. Today sintering is still a very important process for manufacturing of a wide variety of industrial materials. The driving force of sintering is the excess surface free energy of a powder compact. The system tries to decrease its surface free energy by decreasing its total surface area, when they are heated. This achieves by mass transport that joins the powder particles together.

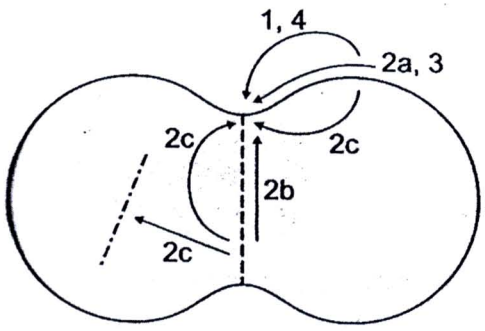

Figure 2.21 Diffusion of different paths during sintering [42].

There is a chemical potential difference between surfaces of dissimilar curvature within the system. A concave surface has a negative free energy, and convex surface a positive free energy. As a consequence, mass transport occurs from the convex surface to the interparticle neck or pore (concave surface). The greater the curvature (the finer the particle size) does, the higher the driving force for sintering. During sintering, mass transport can occur by solid-state, liquid-phase, and vapor-phase mechanisms individually, or in combination (Figure 2.21).

Path 1: *Evaporation-condensation.* Compared to a flat surface, the vapor pressure of a convex surface is higher and that of a concave surface is lower. As a consequence, a substance vaporizes at the convex surface and condenses at the necks and in the pores.

Path 2: Diffusion. The driving forces for diffusion are difference in vacancy concentration. The diffusion mechanisms can be sub-classified into surface diffusion (2a), grain boundary diffusion (2b), and volume diffusion (2c). The driving force for surface diffusion is the difference in vacancy concentration between convex and concave surfaces. The vacancy concentration is lower on a convex surface than that

on a flat surface. On a concave surface is the highest. As a consequence, vacancies flow from a neck (concave area) to a convex area, and thus a mass flow occurs in the reverse direction. Mass flow through the volume of grain (volume diffusion) may originate at convex surfaces, grain boundaries or dislocation in the matrix. Except for substances with high vapor pressure such as NaCl, the sintering of powders proceeds by the volume diffusion mechanism.

Path 3: Flow. A perpendicular pressure pointing to the center of a powder particle acts on a convex surface, and a pressure pointing away from the center acts on a concave surface. When a substance is fluid, mass transport proceeds under the pressure difference.

Path 4: Dissolution-precipitation. In the initial phase of sintering, the presence of a liquid phase which wets the solid phase allows the rearrangement of particle packing by gliding. Subsequently the substance dissolved from convex surface, where solubility is higher, transported to concave surface, where solubility is lower, and precipitates out. Dissolution, precipitation or diffusion in a liquid phase is rate-controlling step.

2.5.1 Stages of sintering

The development of microstructures during sintering is rather complicated, but may be distinguished in three stages as shown in Figure 2.22.

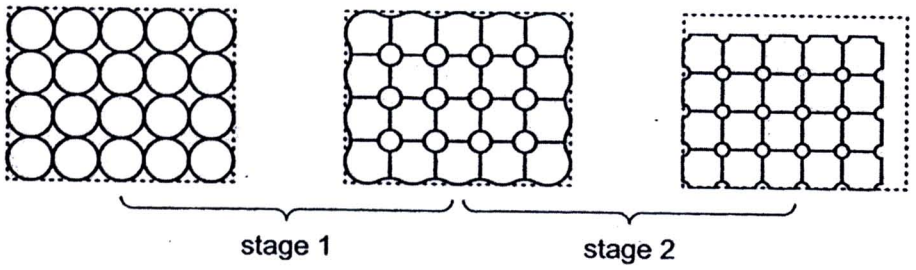

Figure 2.22 A two-dimensional sphere model, illustrating the first two stages during sintering [42].

Initial stage. Initially, material transports from higher-energy convex particle surfaces to the lower-energy concave intersections between adjacent particles to from necks ("neck growth"). The powder particles fuse together and the area of contact increases gradually. Since mass is only transported from convex to concave area. The total pore volume and the distance between the particle centers remain almost at constant, and shrinkage of the green body is only about 4-5 %. In this stage the relative density, which is the density of the powder compact divided by its theoretical density, is about 0.5-0.6.

Intermediate stage. In this stage, interparticle necks grow, the area of gain boundaries (the interface plane shared by two grains) increase, interparticle contacts flatten, and the pore diameters decreases. The distance between the particle centers and the volume of the compacts decrease (shrinkage of 5% to 20%) - densification occurs. The relative density increases to about 0.95.

Final stage. When the relative density increases above 0.95, isolated spherical pore remain only at triple points (intersection lines where three grains meet)

or inside the matrix. In the final stage, these pores are gradually eliminated and the relative density further increases.

2.5.2 Factors affecting sintering

The most important powder physical characteristics that can affect sintering are particle size, particle packing, and particle shape.

Particle size. Material transport occurs faster over shorter distances, and less material needs to be transported to fill small pores. Furthermore, very fine particles have high surface energies. Therefore, smaller powder particles speed up the sintering process and lower the sintering temperature and pressure. Due to the thermodynamic considerations discussed above, larger grains grow at the expense of smaller ones. Consequently, as sintering proceeds, the average size of the grain increase ("coarsening"), and the size distribution becomes smaller. Since coarsening is much slower than sintering, grain growth can occur especially in the final sintering stage. Uncontrolled grain growth is usually detrimental to the ceramics properties.

Particle packing. Improve particle packing increases the number of contact points between adjacent particles and the relative density of the compact. Consequently, densification occurs faster (better material transport) and with less volume shrinkage. One of the most important reasons for non-uniform particle packing is the formation of aggregates.

Particle shape. Irregular-shaped particles, which have a high surface area to volume ratio, have a high driving force for densification, and sintering is faster than equiaxed particles. Particles with poor packing are able to be sintered poorly.

2.5.3 Spark-plasma sintering

Spark plasma sintering (SPS) is a form of sintering where both an external pressure and electric field are applied simultaneously to enhance the densification of the metallic/ceramic powder compacts as shown in Figure 2.29. This densification uses lower temperature and shorter amount of time than typical sintering. Theoretically, there is a high-temperature or high-energy plasma, generated between the gaps of the powder materials, like metals, inter-metallic compounds, ceramics, composites and polymers. Using a DC pulse as the electrical current, spark plasma, spark impact pressure, joule heading, and an electrical field diffusion effect would be created. Certain ceramic materials have low density, chemical inertness, high strength, hardness and temperature capability. Nanocrystalline ceramics have even greater strength and higher superplasticity.

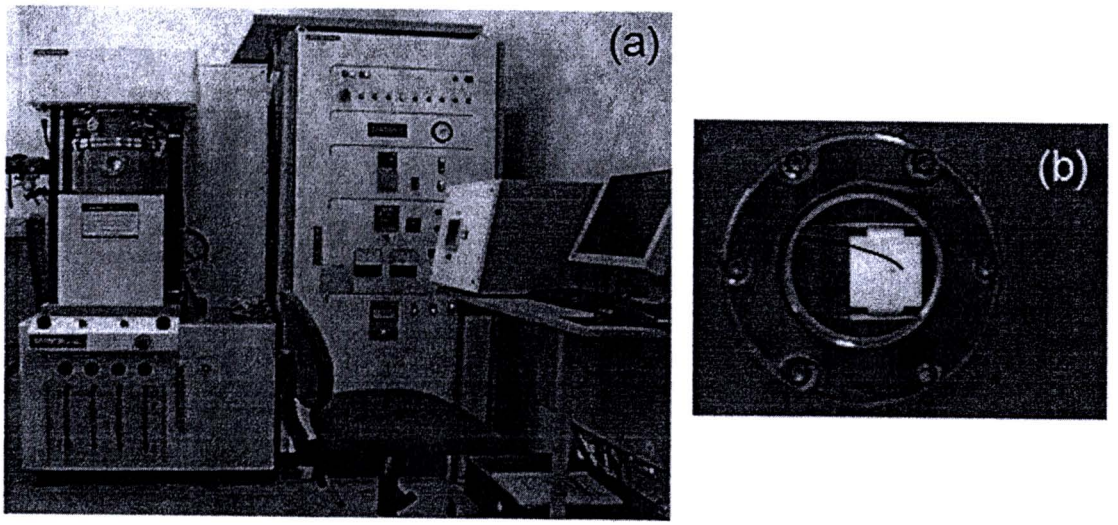

Figure 2.29 (a) Spark plasma sintering system, and (b) graphite die during the SPS operation.

Many microcrystalline ceramics that were treated and had gained facture toughness, lost their strength and hardness, with this many have created ceramic composites to offset the deterioration while increasing strength and hardness to that of nanocrystalline materials. Through various experiments, the mechanical properties of new material can be achieved by controlling the grain size and its distribution, amount of distribution and others. Due to the combination of compaction and temperature, SPS-pressed powders may attain densities of up to >95% of the bulk density. This is extremely useful as a synthesis-measure since many materials are not easily synthesized in bulk form while they are readily obtainable as powders, and yet the properties of interest may only exist in the bulk [44].

2.6 ZnTe

2.6.1 Structure [45]

Zinc telluride is the chemical compound with the ZnTe formula. This solid is an intrinsic semiconductor material with band gap of 2.23–2.25 eV. It is usually a p-type semiconductor as shown in Figure 2.24. Its crystal structure is cubic (Figure 2.25), as both of sphalerite and diamond. Its lattice constant is 0.61034 nm, allowing it to be grown with or on aluminum, antimonide, gallium antimonide, indium arsenide, and lead selenide. It has the appearance of grey or brownish-red powder, or ruby-red crystals when refined by sublimation. Zinc telluride can be prepared as hexagonal crystals (wurzite structure). Table 2.3 shows the property and structure of ZnTe.

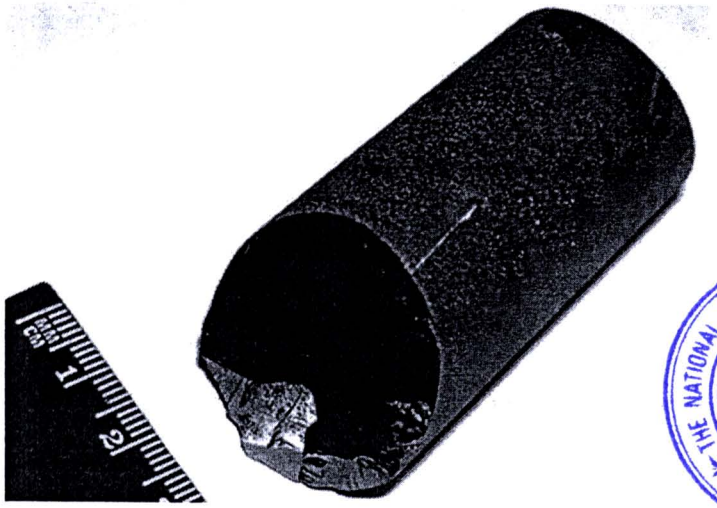

Figure 2.24 ZnTe single crystal [46].

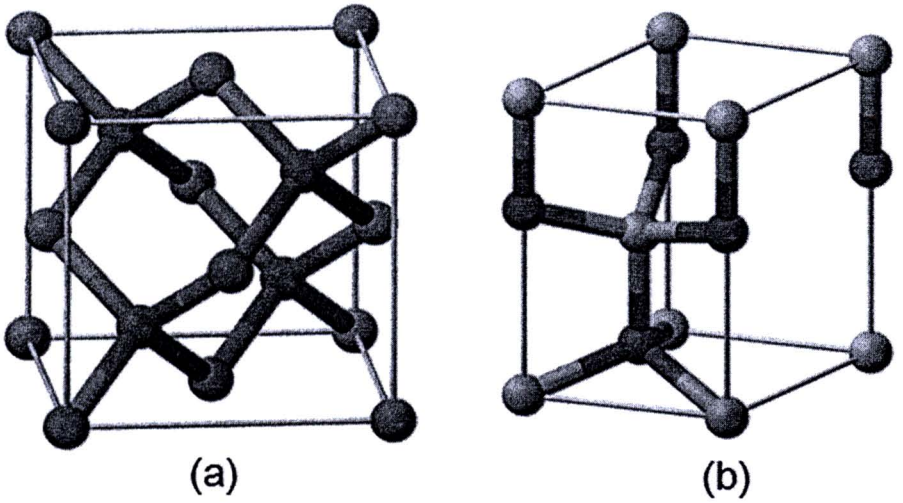

Figure 2.25 The ZnTe structure (a) zinc blende (cubic) [45] and (b) wurtzite [47].

Table 2.3 The property and structure of ZnTe [45].

Properties		**Structure**	
Molecular formula	ZnTe	Crystal structure	Zincblend (cubic)
Molecular mass	193.01 g/mol	Lattice constant	a = 6.1034 Å
Appearance	Red crystal	Coordination	Tetrahedral (Zn^{2+})
Density	6.34 g/cm^3	geometry	Tetrahedral (Te^{2-})
Melting point	1238.5°C		
Band gap	2.23-2.25 eV		

2.6.2 Applications [45]

a) Optoelectronics

Zinc telluride is important for development of various semiconductor devices, including blue LEDs, laser diodes, solar cells, and components of microwave generators. It can be used for solar cells as a background layer and *p*-type semiconductor in PIN structure (e.g. using cadmium telluride; *p*-type or *i*-type (intrinsic) semiconductor, and cadmium sulfide (*n*-type semiconductor). Zinc telluride together with lithium niobate is often used for generation of pulsed terahertz radiation in time-domain terahertz spectroscopy and terahertz imaging. When a crystal of such material is subjected to a high-intensity light pulse of subpicosecond duration, it emits a pulse of terahertz frequency through a nonlinear optical process called optical rectification. Conversely, subjecting a zinc telluride crystal to terahertz radiation

causes it to show optical birefringence (double refraction) and change the polarization of a transmitting light, making it an electro-optic detector.

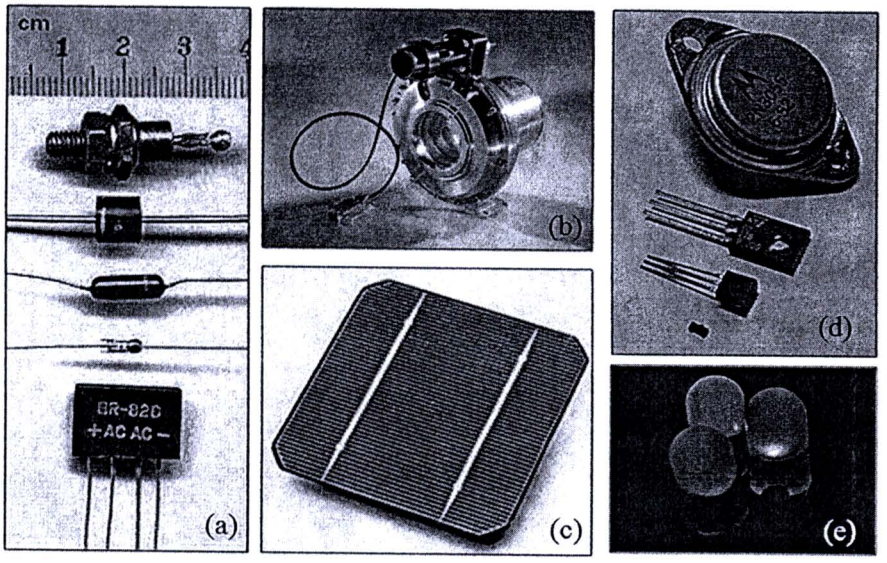

Figure 2.26 The ZnTe applications (a) semiconductor diodes, (b) electro-optics, (c) solar cells, (d) assorted discrete transistors and (e) light-emitting diodes (LED).

b) Electro-optics

Zinc telluride can be easily doped. It is one of the more common semiconducting materials used in optoelectronics. Vanadium-doped zinc telluride, "ZnTe:V", is a non-linear optical photorefractive material of possible use in the protection of sensors at visible wavelengths. ZnTe:V optical emiters are light and compact, without complicated optics of conventional emiters. ZnTe:V can block a high-intensity jamming beam from a laser dazzler, but still passing the lower-intensity image of the observed scene. It can also be used in holographic interferometry, in reconfigurable optical interconnections, and in laser optical phase conjugation

devices. It offers superior photorefractive performance at wavelengths between 600-1300 nm, in comparison with other III-V and II-VI semiconductors. By adding manganese as an additional dopant (ZnTe:V:Mn), its photorefractive yield can be significantly increased.

2.6.3 Synthesis of ZnTe

Bhunia and Bose (1998) have synthesized ZnTe for the first time by microwave heating from high purified Zn and Te, and the minimum reaction time determined to be 30 min. Single crystals were grown by modified vertical Bridgman technique from 4% rich Te melt, the growth direction being found to be the [111]. XRD showed formation of the zinc blende phase with lattice constant 6.106 Å. Inductively coupled plasma (ICP) analysis showed Si, In, Cu, Au, and Fe to be the main impurities present at ppm level. Crystals were p-type with 8.5 Ωcm resistivity, 1.6×10^{16} cm^{-3} hole concentration and 46 cm^2/Vs mobility at 300 K. Mobility was found to vary with temperature as $\mu_p \propto T^{2.7}$ in the range 120-300 K. Photoluminescence (PL) at 10 K showed emission peaks at 2.06, 1.47, 1.33 and 1.05 eV. Thermal quenching of the PL bands has been studied. The samples showed weak photoconductivity due to small minority carrier lifetime. From the temperature dependence of the photoconductive gain, the minority carrier lifetime (τ_n) has been determined in the temperature range of 80-300 K. τ_n was thus found to go through a maximum of 4.5×10^{-7} s at 220 K [9].

Li et al. (2005) have synthesized semiconductor ZnTe nanowire arrays by the pulsed electrochemical deposition from aqueous solution into porous anodic alumina membranes (AAM). High-filling and ordered ZnTe nanowire arrays have

been prepared from aqueous solutions by the pulsed electrochemical deposition into the pores of AAM. The ZnTe nanowires are single-crystalline and have a preferential orientation along the [110] direction. The optical absorption band edge of ZnTe nanowires exhibits a marked blue-shift compared with that of bulk ZnTe due to quantum size effect. ZnTe nanowire arrays were very interesting for applications in optoelectronic and thermoelectric nanodevices in the future [10].

Lee et al. (2007) synthesized highly crystalline zinc telluride (ZnTe) nanocrystals with a controlled shape using various growth conditions. The following amines were used as activation agents for the zinc precursor: zinc stearate, octylamine (OA), dodecylamine (DDA), octadecylamine (ODA), and trioctylamine (TOA). Unique 3-D nanoflowers (av. size = 20-120 nm), consisted of a number of nanodots (av. size = 4-11 nm) were efficiently produced when no amine or TOA was used. Dispersed nanodots were produced when OA, DDA, or ODA were used. These results indicate that the steric effect of alkyl chains plays an important role in the formation of nanoflowers. Furthermore, the shape evolution from nanoflowers to nanorods occurred at higher growth temperatures, and nanoflowers and nanorods eventually evolved into nanodots after incubation [48].

Fanfair et al. (2008) reported the synthesis of ZnE (E = S, Se, Te) nanowires in solution via the solution-liquid-solid (SLS) mechanism. Relatively low nanowire growth temperatures, between 340 and 350 °C, were made possible by using bismuth nanocrystals as seeds. Diethylzinc and zinc(oleate)$_2$ were studied as Zn reactants, and TOP:E complexes were explored as the chalcogen source. The influence of the solvent on the quality and yield of the nanowires was studied with reactions carried out in either the noncoordinating solvent squalane or the coordinating solvents,

trioctylamine (TOA) or trioctylphosphine oxide (TOPO). The solvent and reactant chemistry dramatically affect the yield and quality of the nanowires, with Et_2Zn being more reactive than $Zn(oleate)_2$. The use of coordinating solvents provides a means to optimize nanowire growth [49].

Huang et al. (2008) have synthesized the submicrosized ZnE rods, ZnO/ZnE cables, and ZnE tubes (E = S, Se, Te) via exterior-to-interior boron-chalcogen corrosions on the initial ZnO rods. The morphologies of both ZnE rods and ZnO/ZnE cables are roughly comparable to that of ZnO. The measured optical gaps of the ZnE rods are in agreement with those of the corresponding bulk materials, and the ZnO/ZnE cables exhibit type-I excitonic localization that is restrained in the region of the narrower band gap component [50].

Meng et al. (2008) have synthesized zinc-blende-structured ZnTe nanostructures, periodically twinned nanowires and uniform nanoribbons, by the hydrogen-assisted thermal evaporation method in the presence of Au catalyst via the vapor–liquid–solid (VLS) growth mechanism. The formation of various nano-structures is dependent on the local temperature. The experimental results indicate that twinned nanowires grow along the [111] direction and uniform nanoribbons grow along the [111] and [211] directions. The local temperature of ZnTe growth is the key factor to form various ZnTe nanostructures. Periodically twinned nanowires dominate in the low-temperature zone, whereas uniform nanoribbons dominate in the high-temperature zone. Besides, the transition from the twinned nanowire to the uniform nanoribbon takes place in the middle-temperature zone. EDX analysis and Raman spectrum confirm that twin boundaries are composed of excessive Te layers. Twins or

excessive Te atoms cause slightly red shift of the emission in PL spectrum, which might be potentially used for nanodevices [51].

Guo et al. (2008) have prepared multilayer superstructures of single-crystalline ZnTe nanowire films through a new growth process: well-aligned ZnTe nanowires congregate into nanowire film. The growth process takes place discontinuously and consequently produces many layers of aligned ZnTe nanowire superstructures. These interesting findings are apparently different from the conventional vapor-liquid-solid (VLS) process but following a new multiple nucleation growth model. The characterizations show that the obtained superstructures are composed of uniform single-crystalline ZnTe. The photoluminescence spectrum of the obtained multilayer ZnTe NW superstructures exhibits strong free exciton emission peak and relatively weak line, indicating that the layers are of high quality, which may have potential applications in nanodevices [52].

Tanaka et al. (2003) have clarified the correlation between growth process and layer quality of the ZnTe layers grown on the ZnTe (100) substrates by horizontal metalorganic vapor phase epitaxial (MOVPE) system as a function of the total gas flow rate. The PL spectrum of the ZnTe epitaxial layer grown under the optimum condition was characterized by strong free exciton line and weak excitonic peak attributable to shallow acceptors, indicating high-quality ZnTe layer. From the PL spectrum of this layer, the ground state binding energy of free exciton is found to be 12.7 meV, and the temperature dependence of FE emission was investigated. The resistivity of the layer is determined to be around $5x10^8$ Ωcm using Cox-Strack method, supporting the high crystalline quality layer [53].

Kume et al. (2007) have investigated the homoepitaxial growth of ZnTe on the (100)-oriented ZnTe substrate by horizontal metalorganic vapor phase epitaxial (MOVPE) system at different reactor pressures using dimethylzinc and diethyl-telluride as source materials. The growth rate of ZnTe layers increases with increasing reactor pressure and becomes saturated eventually. The longitudinal optical phonon mode of ZnTe and a strong free exciton emission are clearly observed for all samples, indicating the ZnTe layers are of good crystal quality [54].

Nishio et al. (2001) have investigated the effects of total gas flow rate and transport rate of source materials on the growth rate of ZnTe layers grown on the (100) ZnTe substrates by atmospheric pressure metal organic vapor phase epitaxy (MOVPE). The growth rate increases approximately with the square root of the gas flow rate and then it deviates from this tendency with increasing total gas flow rate. Additionally, the growth rate increases sublinearly with the transport rate of the II and IV group source. Strong free exciton line and excitonic peak attributable to shallow acceptors together with Y bands, characterized the epitaxial films. Through the relationship between the growth process and the layer quality, it was concluded that ZnTe epitaxial layers of good quality were obtainable under the growth conditions close to the mass transport to surface kinetic transition region [55].

Zhang et al. (2008) presented to synthesis nanometer-sized ZnTe by precursor-reduction method. Zinc blende ZnTe nanocrystals growth in three different shapes under various conditions: quasi-spheres, tetrahedrons, and nanorods, have been observed. It is believed that the crystal growth of ZnTe is the rate-controlling step when superhydride was employed at 250°C, resulting in quasi-spherical ZnTe nanocrystals. Replacement of superhydride with oleylamine alters the precursor-

reduction step as the rate-controlling step, giving tetrahedral ZnTe nanocrystals. At low temperature (150°C) and in the presence of superhydride and oleylamine, kinetic growth and/or surfactant-template dominate the process, causing an anisotropic crystal growth into ZnTe nanorods. ZnTe nanocrystals are typically surface-active with a similar crystal structure of CdSe. The present study provides a clue to understand the zinc blende-type nanocrystal growth mechanism in high-temperature colloidal system, and may lighten certain strategies of future nanomaterials processing, for example, the synthesis of one dimensional zinc blende-type semiconductors in solution phase [56].

2.7 Sb_2Te_3

2.7.1 Structure

Bismuth telluride (Bi_2Te_3) and antimony telluride (Sb_2Te_3) have a similar crystallographic structure to bismuth telluride. The rhombohedric structure of antimony telluride belongs to the same space group (R3m) as bismuth telluride. In the hexagonal cell the sequence of stacked layers is

$$-Te^{(1)}-Sb-Te^{(2)}-Sb-Te^{(1)}-$$

The parameters of the hexagonal cell have been determined experimentally by many authors.

$a = 4.25$ Å $\quad c = 29.96$ Å

$a = 4.264$ Å $\quad c = 30.428$ Å

The lamellar structure leads to strong anisotropic of the semiconductor parameters. Infrared transmission investigations have provided an estimate for the forbidden energy gap of between 0.25 and 0.30 eV. The multi-valley type of band structure has been studied by Middendorf et al. [5].

Lengths of bond and angles between bonds in Sb_2Te_3 as shown in Table 2.4 and Figure 2.27 show crystal structure of the thermoelectric Sb_2Te_3 material.

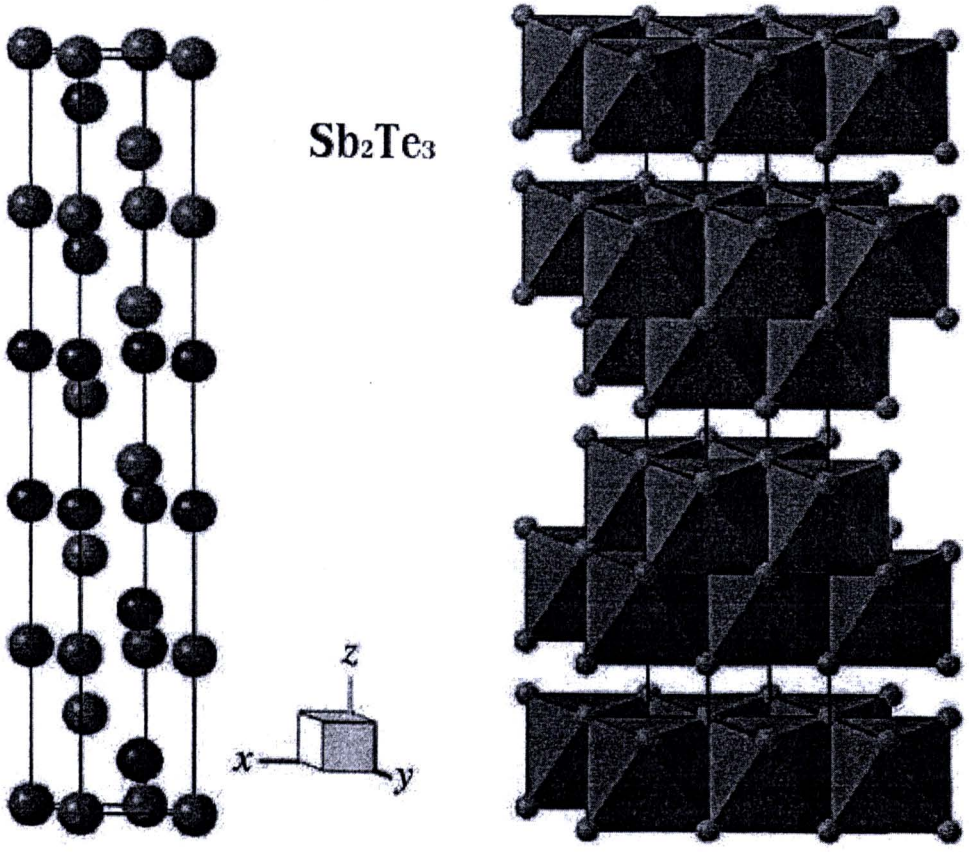

Figure 2.27 Crystal structure of the thermoelectric Sb_2Te_3 material. The blue atoms are Sb and the pink atoms are Te.

Table 2.4 Lengths of bond and angles between bond of Sb_2Te_3 [57].

Bonds	Bond Lengths (Å)	Bond Angles (°)
Sb-Te(1)	2.979	91.4
Sb-Te(2)	3.168	84.6
Te(1)-Te(1)	3.736	69.59

To best assess the recent progress and prospects in thermoelectric materials, the decades of research and development of the established materials should also be considered. By far the most widely used thermoelectric materials are alloys of Bi_2Te_3 and Sb_2Te_3. For near-room-temperature applications, such as refrigeration and waste heat recovery up to 200°C, Bi_2Te_3 alloy has been proved to possess the greatest figure of merit for both *n*- and *p*-type thermoelectric system. Bi_2Te_3 was first investigated as a material of great thermoelectric promise in the 1950s. It was quickly realized that alloying with Sb_2Te_3 and Bi_2Se_3 allowed for the fine tuning of the carrier concentration alongside the reduction in lattice thermal conductivity. The most commonly studied *p*-type compositions are near $(Sb_{0.8}Bi_{0.2})_2Te_3$ whereas *n*-type compositions are close to $Bi_2(Te_{0.8}Se_{0.2})_3$. The electronic transport properties and detailed defect chemistry (which controls the dopant concentration) of these alloys are now well understood to extensive studies of single crystal and polycrystalline materials. Peak *ZT* values for these materials are typically in the range of 0.8 to 1.1 with p-type materials achieving the highest values as shown in Figure 2.28. By adjusting the carrier concentration *ZT* can be optimized to peak at different

temperatures, enabling the tuning of the materials for the specific applications such as cooling or power generating [8].

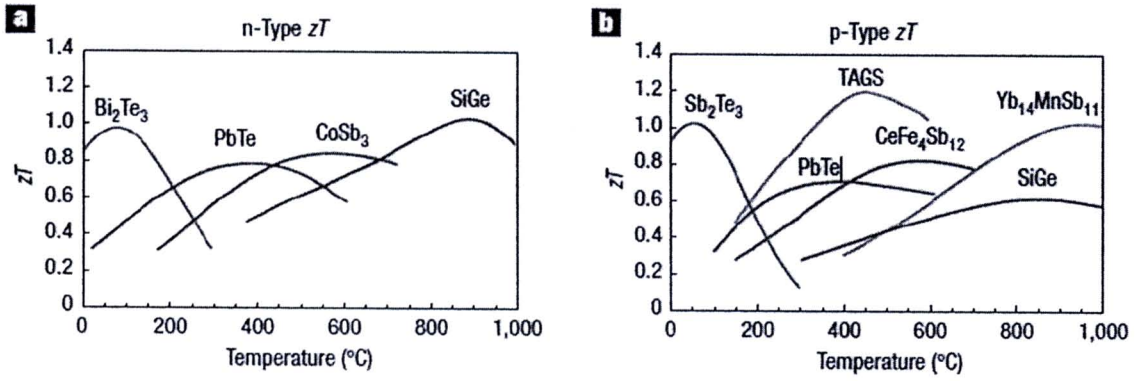

Figure 2.28 Dimensionless figure of merit *ZT* of commercial materials and those used or being developed by NASA for thermoelectric power generation. (a) *n*-type and (b) *p*-type [8].

2.7.2 Synthesis of Sb_2Te_3

Yuan et al. (2007) have successfully fabricated Sb_2Te_3 hexagonal nanoplates via a facile hydrothermal method. These hexagonal nanoplates are typically about 34 nm thick and 300 nm edge long. The production is of good reproducible and holds potential for large-scale synthesis needed for commercial applications. Sb_2Te_3 hexagonal nanoplates hold the potential thermoelectric building block for the possible achieving of high thermoelectric figure of merit due to their novel nanostructure [58].

Wang et al. (2005) have synthesized micrometer-sized hexagonal single-crystlline Sb_2Te_3 nanoplates on a large scale by a solvothermal route. The

experimental results showed that the concentration of CTAB played a key role in the formation of nanoplates. The as-prepared Sb_2Te_3 nanoplates are highly crystallized single crystals. This new nanostructure may have the applications in enhancing the TE performance [59].

Zhou et al. (2008) have developed a simple and rapid microwave-assisted wet chemical routs for the preparation of Sb_2Te_3 hexagonal single-crystalline nanoplates with edge length of hundreds of nanometers. Disproportionating reaction of Te played an important role in the synthesis of Sb_2Te_3, so alkali accelerated the reaction, and the solvents affected the reaction greatly because of the differences in the solubility of NaOH, reducibility, and boiling point. Microwave irradiation was superior to ultrasonic wave and solvothermal process in this synthesis and made the reaction feasible and much faster. PVP was able to regulate and diminish the nanoplates, and it made a difference in the reaction mechanism [60].

Shi et al. (2006) have successfully synthesized the single-crystalline Sb_2Te_3 nanobelts with the length of ca. 200 μm, the width of 1-3 μm, and the thickness of ca. 100 nm by a novel and convenient surfactant-assisted hydrothermal approach. The ionic surfactant AOT acted as the shape controller in the synthetic process. This synthetic route could be applied to obtain other low-dimensional semiconducting telluride nanostructures. Optimizations of the thermoelectric transport properties through assembly or doping of the Sb_2Te_3 nanobelts may lead to novel thermoelectric materials and devices for applications [61].

Zheng et al. (2009) reported thermoelectric properties of MeV Si ion bombarded Bi_2Te_3/Sb_2Te_3 superlattice deposited by magnetron sputtering. In order to keep the stoichiometry of Bi_2Te_3 and Sb_2Te_3, with the purpose of preserving the

electrical and thermal conductivity advantage of the layered structure of bulk Bi_2Te_3 and Sb_2Te_3 in each period of the superlattice. Magnetron sputtering, operated at relatively low temperature, was used to deposit multilayer Bi_2Te_3/Sb_2Te_3 thermoelectric superlattice devices. In addition to the effect of quantum well confinement of the phonon transmission, the nanoscale clusters produced by bombardment of ion beam further adversely affect the thermal conductivity. The increase of the electron density of states in the miniband of nanoscale cluster quantum dot-like structure formed by bombardment also increases the Seebeck coefficient and the electrical conductivity. Eventually, the thermoelectric figure of merit of superlattice films increases [62].

Garje et al. (2006) have demonstrated that $Sb[Te(TeP^iPr_2)_2N]_3$ can be used as a well-defined precursor to rhombohedral Sb_2Te_3 thin films by CVD. Surface analysis of such films confirmed that the growth temperature does not have a profound effect on the morphologies of the deposited film, which are composed of hexagonal nanoplates. This growth technique could also be applied to the synthesis of other semiconductor materials with a range of the interesting nanostructures [63].

Jin et al. (2005) have successfully prepared high-density large-area nanowire arrays of thermoelectric material Sb_2Te_3 using electrochemical deposition into the channels of the porous anodic alumina membrane. They have used a simple direct current electro-deposition process to fabricate large-area Sb_2Te_3 nanowire arrays using PAAM templates. FE-SEM, TEM, and HRTEM investigation results show that the Sb_2Te_3 nanowire arrays are dense, parallel, and large-area, with 100% of the pores of the PAAM templates filled. This simple approach can be generalized to controllably produce a variety of nanowires of interesting nanotechnological

applications. Individual Sb_2Te_3 nanowires are single crystalline and continuous with uniform diameters (~50 nm) throughout the entire length. The atomic ratio of Sb to Te is very close to 2:3 stoichiometric value [64].

Rawat et al. (2000) have studied the effect of argon ion irradiation on vacuum-evaporated as-grown Sb_2Te_3 films in a dense plasma focused device (DPF) by structural, compositional, and morphological analyses. Argon ion irradiation was carried out on as-grown Sb_2Te_3 films. Results show the film contained both stoichiometric and nonstoichiometric phases. Distinct differences were found for samples irradiated at distances less than 8.0 cm from the source (corresponding to ion energies $\geq$ 1 MeV), and those irradiated at distances greater than 8.5 cm ($\leq$ 1 MeV). Ion energy greater than 1 MeV breaks the chemical bonds, resulting in Sb-rich nonstoichiometric phase film. The stoichiometry and morphology of the film was modified by the irradiation of argon ions with energy $\leq$ 1 MeV. The as-grown film containing a considerable amount of nonstoichiometric phase became stoichiometric (Sb_2Te_3) single phase after ion irradiation. This is of great advantage in the use of Sb_2Te_3 films for optical storage applications, especially for those with the possibility of erasability and rewritability. The process of ion irradiation can be used as an intermediary step in storage device fabrication. The preferred orientation of grains and their homogeneous size distribution with stoichiometric single phase should definitely give better figure of merit as a thermoelectric refrigerant, evidenced by the reports in the literature. Therefore, ion irradiation at an energy $\leq$ 1 MeV could be a useful step in the fabrication of both optical storage media and thermoelectric refrigerant using Sb_2Te_3 films grown by simple vacuum evaporation [65].

Arun and Vedeshwar (2003) have measured resistance of vacuum deposited Sb_2Te_3 films of thickness between 100 and 500 nm in vacuum. It was found that the resistance of the polycrystalline films strongly depends on the grain size and intergranular voids. The charge carriers are shown to cross this high resistivity inter-granular void by ohmic conduction. The barrier height as well as temperature coefficient of resistance (TCR) are also shown to depend on the grain size and inter-grain voids. The inter-grain void was controlled by the increasing of grain size, enabling to study the above properties of the films as a function of grain size [66].

Lee et al. (2008) have synthesized nanostructured Sb_2Te_3 and Sb_2Te_3/GeTe core/shell NWs. This approach controls the morphology of the nanostructures and offers a simple method for synthesizing nanostructures with built-in heterojunctions. The Sb_2Te_3 NWs are useful for further study of this phase-change material and the potential applications in electronic memory devices. Similarly, the Sb_2Te_3/GeTe NW heterostructures should be useful for fundamental studies of phase-change materials, such as strain and interface-induced alteration of their phase-change behaviors and material diffusion/doping at the nanoscale. Both Sb_2Te_3 and GeTe grow along the [110] direction with an epitaxial interface between them. Electrical characterization of individual nanowires and nanowire heterostructures demonstrates that these nanostructures exhibit memory-switching behavior [67].

2.8 Ni_3GaSb and Ni_3InSb

Jan and Chang (1991) reported the phases Ni_3AlSb, Ni_3GaSb, and Ni_3InSb existing in their respective ternary systems. The phases exhibit the $B8_{15}$ structure, a partially filled NiAs structure. The phases melt incongruently at >1150 °C, 1066 °C,

and 1091 °C, respectively. This structure is depicted in Figure 2.29. A prominent feature of this structure is the statistical occupation of the lattice sites 2/3, 1/3, 1/4 and 1/3, 2/3, 3/4 by one vacancy and one nickel atom. They are probably not ternary phases, and most likely represent specific compositions of extensive solid solutions of constituent binary phases. The variation in volume with respect to composition of the three phases suggests that they are nearly ideal solutions. Owing to the general similarity between the nickel-metal-antimony and the nickel-gallium-arsenic systems, the Ni_3MSb phases would most likely be the first phases to form in nickel/MSb diffusion couples. Upon consumption of the nickel in nickel/MSb thin-film couples, the Ni_3MSb phases seem to be decomposed into binary phases that were in thermodynamic equilibrium with MSb [68].

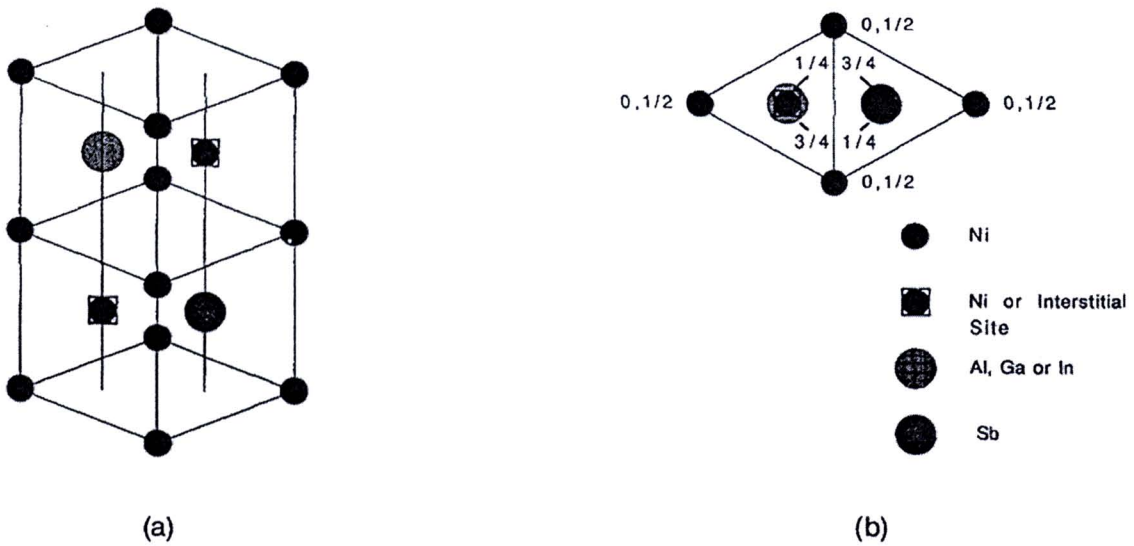

Figure 2.29 (a) Unit cell of the $B8_{1.5}$ structure, (b) Unit cell of the $B8_{1.5}$ structure as viewed along the c-axis [68].